Check for updates

ADVANCED FUNCTIONAL MATERIALS
www.afm-journal.de

Chaotropic Salt-Aided "Water-In-Organic" Electrolyte for Highly Reversible Zinc-Ion Batteries Across a Wide Temperature Range

*Ziqing Wang, Jiefeng Diao, James N. Burrow, Zachary W. Brotherton, Nathaniel A. Lynd, Graeme Henkelman, and Charles Buddie Mullins**

Aqueous zinc-ion batteries are promising alternatives to lithium-ion batteries due to their cost-effectiveness and improved safety. However, several challenges, including corrosion, dendrites, and water decomposition at the Zn anode, hinder their performance. Herein, an approach is proposed, that deviates from the conventional design by adding water into a propylene carbonate-based organic electrolyte to prepare a non-flammable "water-in-organic" electrolyte. The chaotropic salt $Zn(ClO_4)_2$ exploits the Hofmeister effect to promote the miscibility of immiscible liquid phases. Interactions between propylene carbonate and water restrict water activity and mitigate unfavorable reactions. This electrolyte facilitates preferential Zn (002) deposition and the formation of solid electrolyte interphase. Consequently, the "water-in-organic" electrolyte achieves a 99.5% Coulombic efficiency at 1 mA cm^{-2} over 1000 cycles in Zn/Cu cells, and constant cycling over 1000 h in Zn/Zn symmetric cells. A $Na_{0.33}V_2O_5$/Zn battery exhibits impressive cycling stability with a capacity of 175 mAh g^{-1} for 800 cycles at 2 A g^{-1}. Additionally, this electrolyte enables sustainable cycling across a wide temperature range from −20 to 50 °C. The design of a "water-in-organic" electrolyte employing a chaotropic salt presents a potential strategy for high-performance electrolytes in zinc-ion batteries with a large stability window and a wide temperature range.

1. Introduction

Lithium-ion batteries have dominated the market for portable devices and electric vehicles in the past few decades due to their high energy density.[1,2] However, safety issues from the use of flammable organic electrolytes, as well as concerns about supply chains of raw materials, pose a significant challenge to further development.[3–5] Zinc-ion batteries, and predominantly aqueous zinc-ion batteries, have been considered a promising substitute for lithium-ion batteries because of their high theoretical capacity (820 mAh g^{-1}), favorable redox potential (−0.76 V vs standard hydrogen electrode), and increased sustainability due to abundant reserves of Zn.[6–9] More importantly, using water-based electrolytes provides zinc-ion batteries with high safety, low cost, and environmental friendliness.[10–12] However, aqueous electrolytes have resulted in the dissolution of oxide-based cathodes and parasitic reactions (i.e., dendrite formation, hydrogen evolution reaction (HER), and oxygen evolution reaction (OER)) on the anode side, significantly limiting the application of aqueous zinc-ion batteries.[13–17]

Considering these issues originating from the interaction between water and electrodes, reducing the activity of free water molecules in the electrolyte is an effective approach to avoid unfavorable side reactions.[18–21] Consequently, multiple classes of next-generation electrolytes, including molecular crowding electrolytes,[22–24] hydrated eutectic electrolytes,[25–28] aqueous/organic hybrid electrolytes,[29–31] and non-aqueous electrolytes,[32–34] have been developed to optimize battery performance via suppression of water activity and formation of a protective solid electrolyte interphase (SEI). By combining an organic species with only a small amount of water, the above methods mitigate issues related to the presence of water but raise other problems, including high cost, high viscosity, low ionic conductivity, and additional safety risks associated with the flammability of organic constituents.[35] Accordingly, increasing water content in the electrolyte can mitigate the issues arising from the organic component. To avoid reintroducing the deleterious

Z. Wang, J. Diao, G. Henkelman, C. B. Mullins
Department of Chemistry
The University of Texas at Austin
Austin, TX 78712, USA
E-mail: mullins@che.utexas.edu

J. Diao, G. Henkelman
Oden Institute for Computational Engineering and Sciences
The University of Texas at Austin
Austin, TX 78712, USA

J. N. Burrow, Z. W. Brotherton, N. A. Lynd, C. B. Mullins
McKetta Department of Chemical Engineering
The University of Texas at Austin
Austin, TX 78712, USA

C. B. Mullins
Texas Materials Institute and Center for Electrochemistry
The University of Texas at Austin
Austin, TX 78712, USA

The ORCID identification number(s) for the author(s) of this article can be found under https://doi.org/10.1002/adfm.202311271

DOI: 10.1002/adfm.202311271

 © 2023 Wiley-VCH GmbH

consequences of additional water in the electrolyte, intermolecular interactions (e.g., hydrogen bonding) between the organic solvent and water can effectively restrict the water activity and protect electrodes.[36–39] Therefore, developing a co-solvent electrolyte with the appropriate amount of water is necessary to reduce corrosion and dissolution at the anode and cathode, respectively. Nevertheless, because of the differences between the dielectric constant, most organic solvents are insoluble or only slightly soluble in water, which significantly decelerates the development of co-solvent electrolytes.

The Hofmeister effect is a common phenomenon in nature, describing how the solubility of different molecules changes in an aqueous solution with the addition of kosmotropic and chaotropic salts.[39–41] Chaotropic salts, which consist of cations and large monovalent anions with low charge density, can break the hydrogen bonding environment in water and increase the solubility of proteins and other molecules.[42] Although chaotropic salts are able to facilitate the solubility of organic solvents in an aqueous solution due to the Hofmeister effect, their application has rarely been reported so far.[43] Accordingly, introducing a suitable chaotropic salt into a mixture of water and organic species may effectively stabilize and homogenize the liquid system. Inspired by the Hofmeister effect, perchlorate (ClO_4^-), the second most chaotropic anion in the Hofmeister series, is introduced as a solubilizer to form a homogenous co-solvent solution for this study.

As well as changing the composition of electrolytes, anodic surface modification, especially the exposure of the Zn (002) crystalline facet on the anode, has been widely reported to significantly affect Zn deposition and further reduce parasitic reactions.[44–48] For the hexagonal Zn crystal structure, the (002) plane has the lowest surface energy, which restricts side reactions and promotes uniform Zn deposition for a dendrite-free anode via aligning parallel to the Zn surface. Several approaches have been employed to obtain the preferential Zn (002) facet, including mechanical rolling,[49] surface coating,[50] and acid etching.[51] However, the preparation procedures for these pretreatments are too complicated for industrial applicability. Recently, it has been shown that introducing different electrolyte additives can regulate the growth of the (002) facet, resulting in uniform Zn deposition and alleviating parasitic reactions.[46,48] The added molecules preferentially adsorbed on the (002) facet, which hinder the deposition on the (002) plane and facilitate the growth of other facets, eventually exposing the (002) texture. Therefore, achieving preferential deposition of the (002) plane via electrolyte engineering alone could enable a more facile and cost-effective approach than other mechanical and artificial surface-modification methods.

Herein, under the assistance of the $Zn(ClO_4)_2$ chaotropic salt, we introduce an appropriate amount of water into an organic electrolyte ($Zn(ClO_4)_2$/propylene carbonate (PC)) to construct a non-flammable "water-in-organic" electrolyte (WOE). Using $Zn(ClO_4)_2$ significantly promotes the miscibility of water and PC by disrupting the original hydrogen bond networks within each solvent by the Hofmeister effect. The resulting WOE displays a high ionic conductivity and low viscosity comparable to aqueous electrolytes. Meanwhile, the strong intermolecular interaction (hydrogen bonding) between water and PC efficiently confines water activity to further eliminate side reactions. Additionally, experimental evidence supported by density functional theory (DFT) calculations indicates the preferential adsorption of PC molecules on the Zn surface to regulate the exposure of the Zn (002) facet, leading to uniform Zn deposition. Further, adsorbed PC molecules are electrochemically reduced into a SEI comprised primarily of $ZnCO_3$ and $Zn_5(CO_3)_2(OH)_6$ that passivate the Zn anode from parasitic reactions (i.e., HER) and facilitate the interfacial reaction kinetics. Accordingly, Zn plating/stripping in WOE exhibits impressive reversibility and stability with a Coulombic efficiency (CE) of 99.5% at 1 mA cm^{-2} to a plated capacity of 0.5 mAh cm^{-2} for 1000 cycles in Zn/Cu cells and a cycling performance at 1 mA cm^{-2} over 1000 h in Zn/Zn symmetric cells. A $Na_{0.33}V_2O_5$/Zn full cell battery achieves an average capacity of 175 mAh g^{-1} for 800 cycles at 2 A g^{-1} without capacity decay. Furthermore, due to the modified chemical environment and H-bond network in the electrolyte, both the symmetric and full cells in WOE demonstrate high reversibility and stability across a wide temperature range from −20 to 50 °C. This study emphasizes that the use of "water-in-organic" electrolytes with chaotropic salt provides a promising strategy for achieving high-performance zinc-ion batteries across a wide temperature range.

2. Results and Discussion

2.1. Structure of "Water-In-Organic" Electrolyte

Propylene carbonate (PC), a conventional solvent for lithium-ion battery electrolytes with a high dielectric constant and good electrochemical stability, was selected as the organic co-solvent in this work.[52–54] However, water and PC solvent are hardly miscible. A mixture of water and PC (prepared by adding 30 wt.% of water to the PC solvent) exhibited a phase separation, indicating very poor compatibility between PC and water (Figure S1a, Supporting Information). Hence, it is necessary to select a salt as the "link" to make water and PC solvents miscible. As shown in Figure S2 (Supporting Information), the commonly used zinc salts, including $ZnCl_2$, $Zn(NO_3)_2$, $Zn(Ac)_2$, $ZnSO_4$, and $Zn(OTf)_2$, do not dissolve in the PC solvent. However, $Zn(ClO_4)_2$ can be easily dissolved in PC, forming a transparent liquid due to perchlorate's low association with Zn^{2+} caused by the poor complexing ability.[55] Therefore, considering that $Zn(ClO_4)_2$ is soluble in both PC and water, and the perchlorate (ClO_4^-) is the second most chaotropic anion in the Hofmeister series, $Zn(ClO_4)_2$ chaotropic salt serves as a "solubilizer" to break the original chemical environment in the PC and water solutions to facilitate the miscibility of both solvents in the electrolyte mixture. Specifically, ClO_4^- can break the original H-bond networks in both water and PC, thereby allowing them to coordinate with each other via intermolecular interactions.[42] Consequently, the initially phase-separated liquid becomes homogeneous after the addition of the $Zn(ClO_4)_2$ chaotropic salt (Figure S1b, Supporting Information). The phenomenon of promoting mutual solubility between initially immiscible solvents with different polarities by adding salt can be attributed to the Hofmeister effect, which makes it possible to add an arbitrary amount of water into a $Zn(ClO_4)_2$/PC organic electrolyte.[40,56]

The co-solvents (total mass: 1 g) of PC and water with varied mass ratios (i.e., 9:1, 8:2, 7:3, 6:4, and 5:5) were mixed

© 2023 Wiley-VCH GmbH

16163028, 0, Downloaded from https://onlinelibrary.wiley.com/doi/10.1002/adfm.202311271 by Northwestern University Libraries, Wiley Online Library on [15/12/2023]. See the Terms and Conditions (https://onlinelibrary.wiley.com/terms-and-conditions) on Wiley Online Library for rules of use; OA articles are governed by the applicable Creative Commons License

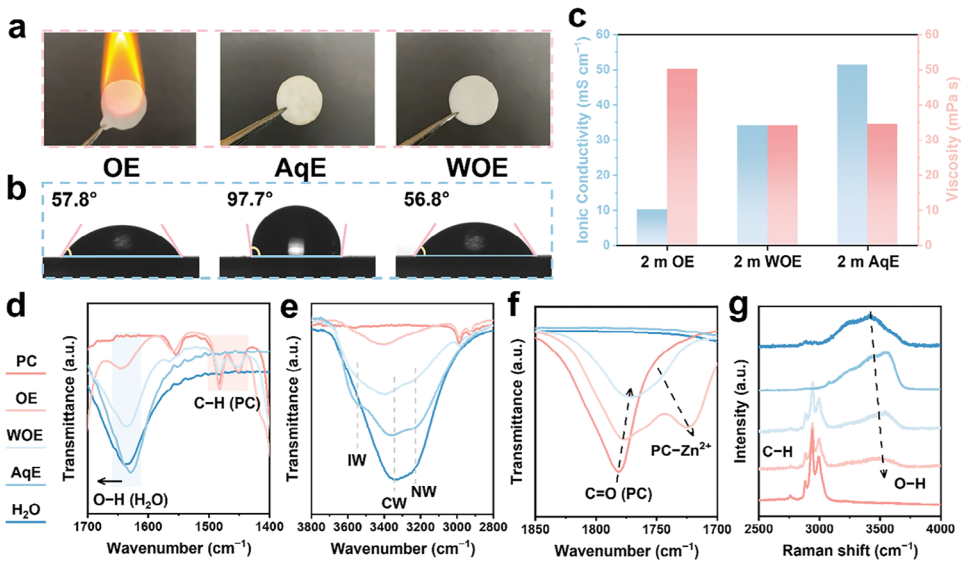

Figure 1. Characterization results of different electrolytes. a) Ignition tests of separators with saturated OE solution, AqE solution, and WOE solution. b) Contact angle tests of OE, AqE, and WOE on the pristine Zn metal surface. c) Ionic conductivity and viscosity profiles of OE, AqE, and WOE. d–f) ATR-FTIR and g) Raman spectra of PC, H_2O, and different electrolytes with 2 m concentration.

with 0.002 mol $Zn(ClO_4)_2$ to form "water-in-organic" electrolytes with concentrations of 2 mol $kg^{-1}_{solvent}$ (m). For a comparison, 0.002 mol $Zn(ClO_4)_2$ was added to 1 g PC to form an organic electrolyte (2 m OE) and 1 g water to form an aqueous electrolyte (2 m AqE). Although pure organic electrolytes are combustible, hybrid electrolytes with sufficient water content can demonstrate diminished flammability.[57] A piece of glass fiber separator cannot be ignited by a flame; however, after soaking in the organic electrolyte, it ignited immediately when exposed to a flame (Figure S3, Supporting Information). In contrast, the electrolyte-soaked glass fiber separators show non-flammability when the water content reaches 40 wt.% (**Figure 1**a; Figure S3, Supporting Information). Accordingly, the water-in-organic electrolyte with a weight ratio of 6:4 is identified as the optimal electrolyte in this work (denoted by 2 m WOE).

The physicochemical properties of electrolytes influence the electrochemical performance. Contact angle measurements were conducted to evaluate the wettability between Zn foils and 2 m OE, AqE, and WOE (Figure 1b). Contact angle results indicate that AqE exhibits the largest contact angle (97.7°), while both OE and WOE show decreased contact angle values (57.8 and 56.8°, respectively), demonstrating the lower surface energy of the interfaces between Zn foils and the electrolytes with increased organic character. Such increased wettability could enhance the interfacial Zn^{2+} transport dynamics in WOE and OE compared with AqE, which decreases the energy barrier for Zn nucleation.[58,59] In addition to the comparable wettability of WOE and OE with Zn metal, due to the additional water content, the WOE exhibited a smaller viscosity (approaching the value of the pure AqE) and a nearly three-times increase in ionic conductivity as compared to the pure OE (Figure 1c; Figures S4 and S5, Supporting Information), indicating that WOE offers enhanced physicochemical properties as a promising electrolyte for zinc-ion batteries. Moreover, WOE displays a higher Zn^{2+} transference number (0.69) in comparison with AqE (0.49), indicating that Zn^{2+} dominates ion conduction in the WOE (Figure S6, Supporting Information). The limited migration of ClO_4^- anion in the WOE reduces the movement of anions to the Zn anode surface and further suppresses undesirable side reactions.[60–62]

To investigate intermolecular interactions within the electrolytes, attenuated total reflectance Fourier transform infrared (ATR-FTIR) and Raman spectroscopies were conducted (Figure S7, Supporting Information). Figure 1d shows the O—H bending vibration mode of water molecules in OE, AqE, and WOE. Compared with AqE, the O—H bending mode blueshifts from 1629.5 to 1635.4 cm^{-1} in WOE, which can be attributed to the interaction (i.e., hydrogen bonding) between H in water and O of C=O double bond in PC (C=O—H—O). Two lone pairs of electrons in the O atom of the C=O accept sufficient H bonds to confine the free water molecules.[63] In addition, a slight peak in the OE spectrum can be ascribed to the absorbed atmospheric water when the OE was exposed to air during the measurement. This peak also shifts to a higher wavenumber than AqE (1639.2 cm^{-1}). An additional O—H stretching broadband in the region between 2800 and 3800 cm^{-1}, consisting of three types of components corresponding to the water molecules with various chemical environments, provides further information about the electrolyte dynamics (Figure 1e). Three water types are: 1) network water (NW) with a tetrahedral arrangement linked by H bonds (3250 cm^{-1}); 2) clustered water (CW) with H bonded water clusters (3350 cm^{-1}); and 3) isolated water (IW) without interaction with other water molecules (3550 cm^{-1}).[64,65] Compared to AqE, it is clear that the clustered water (CW), which has weak H bonds, exhibited a significant decrease upon the addition of PC in WOE, demonstrating a reduction of H-bonded water molecules and aggregated water clusters. Moreover, the band at 3250 cm^{-1} decreased with the introduction of PC in WOE, supporting the notion that H-bonded water networks are weakened by the substantial H-bond acceptor (C=O double bond in PC molecules).[66] Furthermore,

© 2023 Wiley-VCH GmbH

16163028, 0, Downloaded from https://onlinelibrary.wiley.com/doi/10.1002/adfm.202311271 by Northwestern University Libraries, Wiley Online Library on [15/12/2023]. See the Terms and Conditions (https://onlinelibrary.wiley.com/terms-and-conditions) on Wiley Online Library for rules of use; OA articles are governed by the applicable Creative Commons License

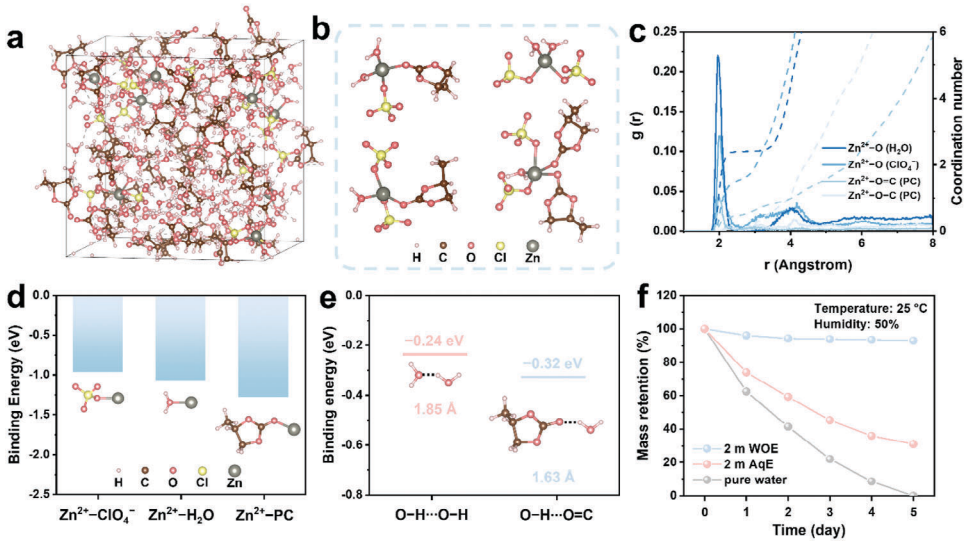

Figure 2. DFT-MD calculation results of WOE. a) A snapshot of the DFT-MD simulation of the electrolyte structure in WOE, and b) corresponding four typical solvation structures. c) RDFs and coordination number of WOE. d) The binding energies of Zn^{2+} with H_2O, ClO_4^-, and PC. e) H-bond binding energies of HOH•••O (H_2O) and HOH•••O (PC). f) Plot of mass retention for 1 mL of different electrolytes in the air under a temperature of 25 °C and a humidity of 50% with the exposed surface area of 3 cm^2.

these O—H stretching vibrations (corresponding to NW and CW) shifted toward higher wavenumbers in WOE than in AqE, again verifying that the introduction of PC disrupts the H bond network between water molecules.[67] In agreement with the FTIR results, the Raman spectrum revealed a blueshift and an obvious decrease in intensity for the band associated with O—H stretching modes between 2500 and 4000 cm^{-1} as compared to AqE, further indicating a change of coordinating environment and interaction between water molecules due to the addition of PC in the hybrid electrolyte (Figure 1g). ^1H NMR measurements further demonstrated that PC breaks the H-bond between free water molecules. As shown in Figure S8 (Supporting Information), the chemical shift of protons from water is observed at 4.71 ppm in AqE but shifts downfield to 4.72 ppm in WOE, demonstrating that the H-bond between PC and water reduces the solvation ability of water around Zn^{2+}. These results illustrate that the PC molecules in WOE serve as H-bond acceptors, effectively bonding with free water molecules and confining their activity. Besides this information on O—H vibrational states, an additional mode at 1781.9 cm^{-1} in the FTIR spectrum of pure PC can be assigned to the C═O vibration (Figure 1f). Upon the addition of $Zn(ClO_4)_2$, this C═O vibration shifts toward lower wavenumbers in both OE (1778.1 cm^{-1}) and WOE (1776.1 cm^{-1}), indicating that PC interacts with water and Zn^{2+}. Moreover, an obvious new band appearing at a lower wavenumber in the OE compared to the pure PC solvent represents the coordination between Zn^{2+} and PC molecules. These results imply that PC directly participates in the solvation structure of Zn^{2+} ions.[68] A similar feature to this peak is observed in WOE, confirming that PC molecules coordinate with Zn^{2+} ions.

To further investigate the solvation structure of Zn^{2+} and molecular interactions in the electrolyte, DFT molecular dynamics (DFT-MD) simulations were performed (**Figure 2**a; Figure S9a, Supporting Information). In WOE, water, ClO_4^-, and PC can be found in the primary solvation shell (Figure 2b), and the average coordination numbers of water and PC with Zn^{2+} are 2.5 and 1.0, respectively (Figure 2c). However, in AqE, three or four water molecules coordinate with Zn^{2+} in the first solvation sheath (Figure S9b,c, Supporting Information). These results imply that PC molecules compete with water to coordinate with Zn^{2+}, likely due to its relatively larger coordination energy (Figure 2d). Further, despite the 7:1 molar ratio of water: PC in the bulk electrolyte, the water: PC ratio in the solvation structure was 2.5:1 as a result of this competition for solvation. Decreasing the water content in the solvation structure mitigates side reactions at the anode surface related to water decomposition.[21,27,69] In addition to coordinating with Zn^{2+}, PC also forms H-bonds with free water molecules in the bulk (non-solvating) electrolyte and reduces water activity. In fact, the H-bond between PC and water (−0.32 eV) was calculated to be stronger than that between water molecules (−0.24 eV) (Figure 2e). Furthermore, the decrease in water activity was experimentally confirmed by the mass retention of electrolytes after equilibration (i.e., evaporation) to a headspace of 50% humidity. After being exposed to a constant atmosphere (50% humidity and 25 °C) for five days, all the pure water evaporated, and the retention of AqE dropped to 30% (Figure 2f). In contrast, WOE retained 94% of its mass, supporting the idea that water activity is significantly limited by the H-bond provided by PC molecules.

2.2. Investigation of Zn/Zn^{2+} Redox Reactions and Zn Deposition

Linear sweep voltammetry (LSV) measurements of Zn/stainless steel cells were conducted to initially evaluate the electrochemical stability window of the electrolytes. Figure S10 (Supporting Information) displays an expanded onset potential of −0.25 V in WOE at the reduction side as compared to −0.12 V in AqE. Similarly, the oxidation side exhibits an increased potential of 2.51 V in WOE, which was nearly 0.5 V higher than in AqE (2.02 V).

© 2023 Wiley-VCH GmbH

16163028, 0, Downloaded from https://onlinelibrary.wiley.com/doi/10.1002/adfm.202311271 by Northwestern University Libraries, Wiley Online Library on [15/12/2023]. See the Terms and Conditions (https://onlinelibrary.wiley.com/terms-and-conditions) on Wiley Online Library for rules of use; OA articles are governed by the applicable Creative Commons License

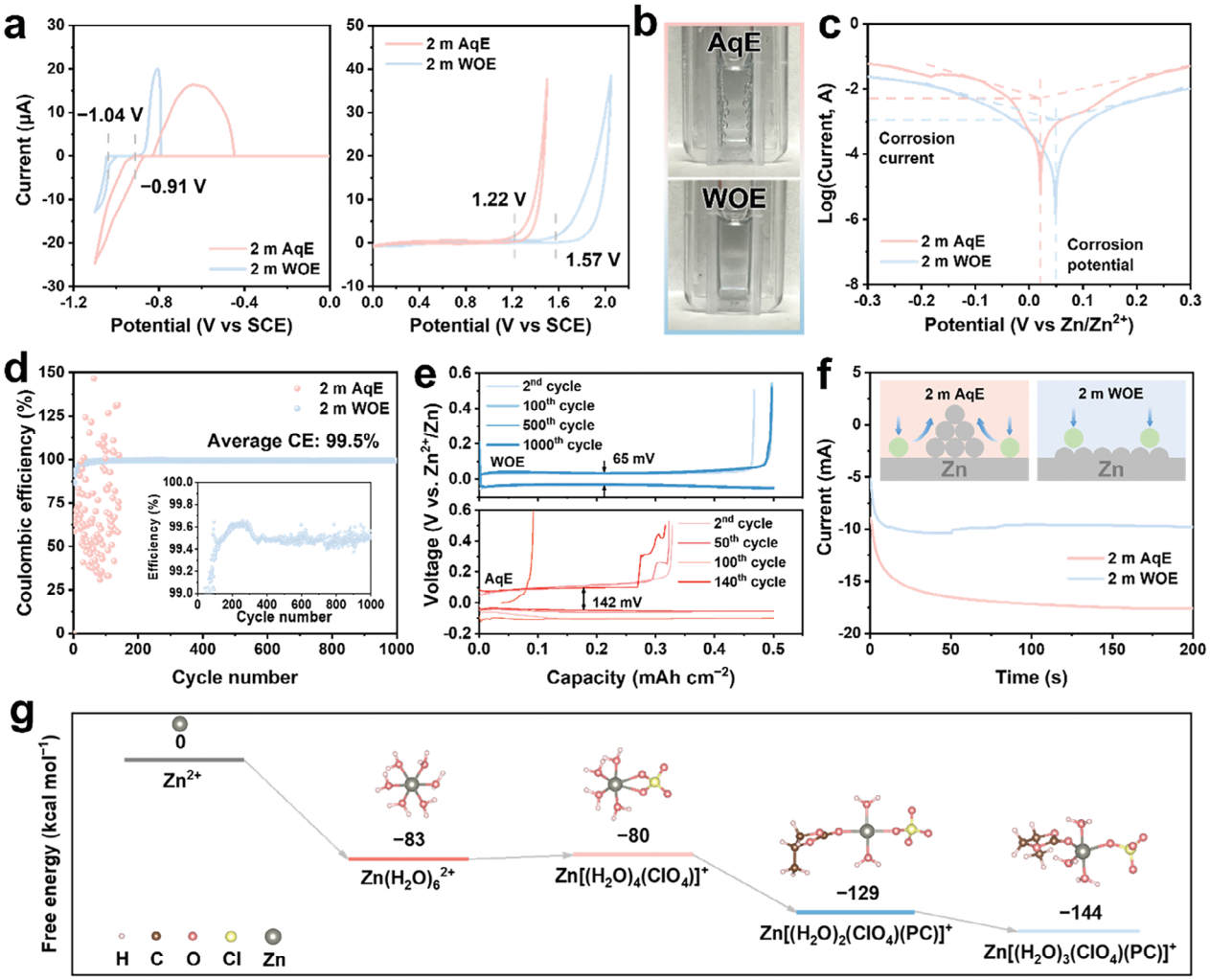

Figure 3. Reversible and stable Zn plating/stripping behavior. a) CV curves of Pt microelectrode/Pt wire symmetric cells within 2 m AqE and WOE. b) Optical Zn/Zn symmetric cuvette cells in AqE and WOE after ten cycles. c) Tafel plots of Zn metal in AqE and WOE in Zn/Cu half cells. d) CE of Zn plating/stripping performance on Cu foils in Zn/Cu half cells at 1 mA cm^{-2} to a capacity of 0.5 mAh cm^{-2} and e) corresponding voltage profiles at different cycles in AqE and WOE. f) CA measurements of Zn/Cu half cells at a −200 mV overpotential. g) Free energy change of the desolvation process in different Zn^{2+} solvation structures.

However, LSV measurements with fast scan rates could lead to an overestimation of the electrochemical stability window by hiding the current produced by the formation of byproducts. Additionally, the difference in water content between WOE and AqE could not be ignored as it could have a dominant role in enlarging the electrochemical window.[70,71] Therefore, cyclic voltammetry (CV) measurements at a slow scan rate were carried out to evaluate the electrochemical window. A Pt microelectrode was utilized as the working electrode to eliminate the influence of mass transfer and maintain the measurement under steady-state conditions. As shown in **Figure 3**a, similar to the LSV results, the electrochemical window was extended from 2.26 V in AqE to 2.61 V in the WOE. The enlarged stability window can be ascribed to the confined water activity induced by the PC molecules, which reduced the kinetic factors.[70] Notably, the CV results only provide a narrow window of 2.61 V compared to the LSV result (2.76 V), indicating the electrochemical window determined by LSV was overestimated with the larger electrodes and faster scan rates. More intuitive evidence of the suppression of OER and HER is provided by the digital photographs of Zn/Zn symmetric cuvette cells after ten electrochemical cycles (Figure 3b). On the Zn electrodes, a large quantity of bubbles was observed in AqE but absent in the WOE after cycling, illustrating a suppression of HER and OER in WOE. The mitigation of OER and HER is most likely due to both the confined water activity in the bulk electrolyte and the limited amount of water in the Zn^{2+} solvation structure in the WOE. Tafel plots of AqE and WOE verify the alleviation of corrosion of the Zn anode due to reduced water activity. As depicted in Figure 3c, the WOE exhibits a lower corrosion current (1.15 mA) and higher corrosion potential (0.05 V) than the AqE (5.26 mA and 0.02 V), reflecting better anti-corrosion properties in the WOE.

Zn plating/stripping on Cu foil was conducted to assess the reversibility and CE of Zn/Zn^{2+} redox reactions in the Zn/Cu

© 2023 Wiley-VCH GmbH

16163028, 0, Downloaded from https://onlinelibrary.wiley.com/doi/10.1002/adfm.202311271 by Northwestern University Libraries, Wiley Online Library on [15/12/2023]. See the Terms and Conditions (https://onlinelibrary.wiley.com/terms-and-conditions) on Wiley Online Library for rules of use; OA articles are governed by the applicable Creative Commons License

16163028, 0, Downloaded from https://onlinelibrary.wiley.com/doi/10.1002/adfm.202311271 by Northwestern University Libraries, Wiley Online Library on [15/12/2023]. See the Terms and Conditions (https://onlinelibrary.wiley.com/terms-and-conditions) on Wiley Online Library for rules of use; OA articles are governed by the applicable Creative Commons License

half-cell batteries. In AqE, the sporadic and unstable CE observed upon cycling may be attributed to both the severe parasitic reactions caused by water and the growth of Zn dendrites (Figure 3d). In the OE, the CE remains stable for 300 cycles and then fluctuates for the subsequent 300 cycles with an average value of 91.4%, which may be related to the high viscosity and low ionic conductivity of OE (Figure S11, Supporting Information). In contrast, WOE maintains an average CE of 99.5% for 1000 cycles and a constant overpotential of 65 mV for Zn plating/stripping, less than half of the 142 mV overpotential required in AqE (Figure 3e). Moreover, compared to WOE, both OE and AqE exhibit lower average CEs and more obvious fluctuation (Figure S12, Supporting Information), clearly indicating that the WOE enables highly efficient and reversible Zn electrodeposition, mainly by suppressing water decomposition and modulating the solvation structure and ionic conductivity.

Chronoamperometry (CA) was performed in the Zn/Cu half cells with an applied overpotential of −200 mV versus Zn/Zn^{2+} to further evaluate the nucleation and electrodeposition behavior of Zn on the Cu foils. The CA plot of AqE shows a continuous current increase beyond 200 s, while WOE shows a short-time increase of current for 50 s with a subsequent current decrease until stabilization (Figure 3f). In AqE, Zn^{2+} ions tend to diffuse on the surface to deposit on the favorable nucleation sites (existing Zn nuclei), which need a higher current to provide the driving force to overcome the diffusional energy barrier. In contrast, due to the hindrance provided by PC molecules on the electrode surface, uniform Zn deposition occurs where Zn^{2+} ions adsorb without additional diffusion, which requires a small amount of energy and low current. To further investigate Zn nucleation and deposition and visualize Zn deposition, 5 mAh cm^{-2} Zn was deposited on Cu foil under a current density of 1 mA cm^{-2} in Zn/Cu half cells. Figure S13 (Supporting Information) indeed shows severe Zn aggregation occurred in the AqE with the apparent formation of Zn dendrites. In contrast, WOE enabled a more uniform Zn deposition. Scanning electron microscope (SEM) and 3D topography images of the Zn deposited on Cu foil in AqE verify the formation of Zn dendrites on the surface. In contrast, dense and uniformly distributed Zn deposition is observed in WOE in agreement with previous CA analysis results. Further, cross-sectional SEM images demonstrate the uneven deposition and Zn dendrites in AqE but homogeneous plating in WOE (Figure S14, Supporting Information).

Furthermore, CV and galvanostatic tests were applied to analyze the dynamics of Zn electrodeposition on Cu foil in AqE and WOE. For the first cycle of CV measurements, the onset overpotential during the negative (cathodic) scan in WOE is 50 mV higher than in AqE, indicating suppressed HER activity in WOE (Figure S15, Supporting Information). Nucleation overpotentials (η_n) were measured in Zn/Cu cells under galvanostatic Zn electrodeposition on Cu foil. Figure S16 (Supporting Information) suggested that the WOE requires a 45 mV higher nucleation overpotential (η_n) than AqE. Based on Young's equation and Fowkes equation, the relationship between nucleation overpotential and nucleation radius can be summarized as:[72–74]

$$r = \frac{3V_m\gamma_{sg}}{F|\eta_n|} \times \left(\frac{1-\cos\theta}{1+\cos\theta}\right)^2 \quad (1)$$

where r is the radius of the Zn nuclei, V_m is the molar volume of Zn, γ_{sg} is the surface energy of the substrate, F corresponds to the Faraday constant, and η_n represents nucleation overpotential. According to the above equation, the larger nucleation overpotential and the smaller contact angle between electrolyte and electrode can simultaneously reduce the size of Zn nuclei. Compared with AqE, WOE exhibits a 40 mV larger overpotential and a smaller contact angle, indicating that smaller and more uniform nucleation sites tend to form in WOE. Moreover, the larger Zn growth overpotential (η_g) in WOE indicates that desolvation in WOE requires more energy, likely due to the stronger interaction between Zn^{2+} and PC (Figure 2d).[75] To further evaluate differences in the solvation structures in the AqE and the WOE, desolvation energies were computed with DFT. As shown in Figure 3g, the desolvation process of $Zn(H_2O)_6^{2+}$ requires overcoming an energy barrier of 83 kcal mol^{-1}. In the AqE, the desolvation energy of $Zn[(H_2O)_4(ClO_4)]^+$ only exhibits 80 kcal mol^{-1}, which is lower than $Zn(H_2O)_6^{2+}$. However, the solvation structures with PC molecules need significantly larger energy for desolvation (e.g., 129 and 144 kcal mol^{-1}), consistent with the observed increased growth overpotential (η_g) for Zn plating/stripping in the above results.

2.3. Electrochemical Performance and Characterization of Zn/Zn Symmetric Cells

Sustained cycling of Zn/Zn symmetric cells was conducted to investigate the stability and reversibility of Zn plating/stripping. As shown in **Figure 4**a, a short circuit occurred in the AqE at around 200 h under a low current density of 0.5 mA cm^{-2}, while the Zn/Zn symmetric cell in the WOE can cycle stably for at least 1000 h under the same current density. Moreover, the inset Figures demonstrate a similar overpotential and Zn plating/stripping behavior in the WOE at different cycling periods, confirming the highly reversible cycling behavior in the WOE. Similarly, at 1 mA cm^{-2}, symmetric cells employing WOE cycled consistently over 1000 h without notable fluctuations in the overpotential, whereas the cells with the AqE exhibited poor stability and only 100 h of cycling (Figure 4b). Variable rate cycling indicated reversible and stable Zn plating/stripping in the WOE under both small and large current densities (Figure S17, Supporting Information). In contrast, the AqE could not tolerate a high current density of up to 5 mA cm^{-2}, as short circuits were observed in the following cycles. Long-term cycling at 5 mA cm^{-2} further confirmed the superior stability of the WOE at large current densities (Figure S18, Supporting Information). Furthermore, as depicted in Figure S19 (Supporting Information), the Zn/Zn batteries exhibit sustainable cycling in WOE even under high current densities (5 and 10 mA cm^{-2}) to achieve high areal capacities (5 and 10 mAh cm^{-2}). In contrast, the Zn/Zn symmetric cells experienced short circuits under similar conditions within the AqE due to the massive formation of Zn dendrites and byproducts caused by water decomposition in the AqE.

The morphological differences of the post-cycled Zn electrodes in AqE and WOE were characterized by visualization techniques. As shown in Figure 4c, Zn dendrites could be observed in the SEM image of the tested electrode in AqE. The cross-sectional SEM image and 3D topography image also confirmed

 © 2023 Wiley-VCH GmbH

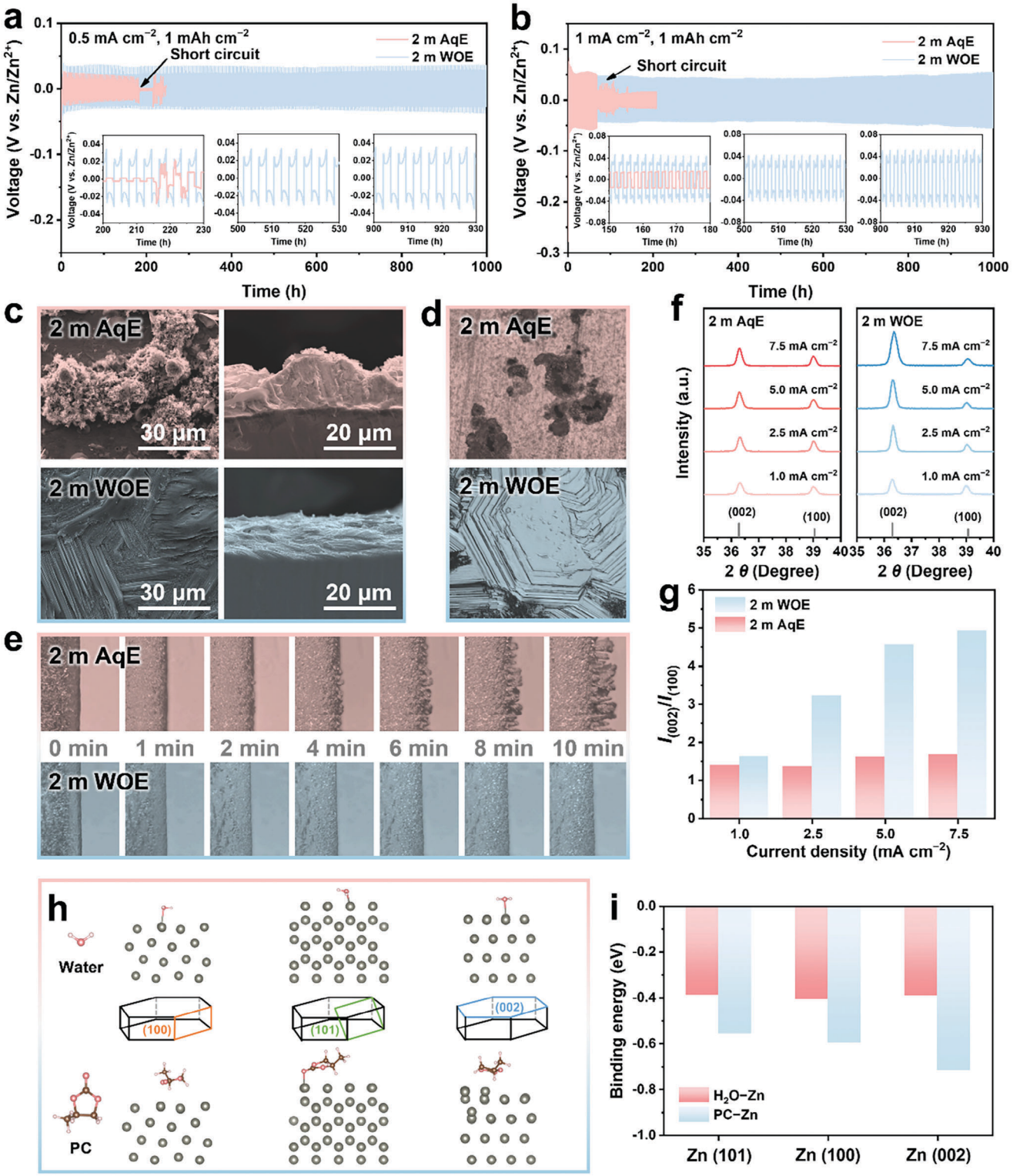

Figure 4. Highly reversible Zn plating/stripping behavior and mechanism of uniform Zn deposition. Cycling performance of Zn/Zn symmetric cells under current densities of a) 0.5 mA cm^{-2} and b) 1 mA cm^{-2} to a capacity of 1 mAh cm^{-2}. c) SEM and d) 3D topography images of Zn foils after depositing 5 mAh cm^{-2} of Zn in AqE and WOE. e) In situ optical images of Zn/Zn symmetric optical cells at 2 mA cm^{-2}. f) XRD patterns at the region of 35–40° of Zn deposited Cu foils with a deposition capacity of 5 mAh cm^{-2} at different current densities in AqE and WOE. g) Corresponding ratios of peak intensities between (002) and (100) facets. h) The adsorption states of water and PC on different crystalline facets of Zn metal, and i) the corresponding adsorption energy of water and PC on different crystalline facets.

© 2023 Wiley-VCH GmbH

16163028, 0, Downloaded from https://onlinelibrary.wiley.com/doi/10.1002/adfm.202311271 by Northwestern University Libraries, Wiley Online Library on [15/12/2023]. See the Terms and Conditions (https://onlinelibrary.wiley.com/terms-and-conditions) on Wiley Online Library for rules of use; OA articles are governed by the applicable Creative Commons License

the formation of Zn dendrites and pits when tested within AqE (Figure 4c,d; Figure S20a, Supporting Information). In contrast, the SEM image of the deposited Zn foil within WOE reveals a uniform surface with hexagonal Zn plates stacked parallel to the substrate, reinforced by the cross-sectional image with the flat surface of Zn foil (Figure 4c). Further, the 3D morphology mapping demonstrates hexagonal Zn platelets stacked parallel to the Zn substrate, corresponding to the (002) facet of the Zn metal crystal (Figure 4d; Figure S20b, Supporting Information). Figure S21 (Supporting Information) illustrates two different deposition modes in the AqE and the WOE. In the AqE, single hexagonal Zn plates are prone to aggregate on the substrate randomly, which may accumulate as Zn dendrites (Figure S21b, Supporting Information), while hexagonal Zn plates mainly deposit parallel to expose the (002) plane in WOE (Figure S21c, Supporting Information). Moreover, optical cells exhibit distinct Zn deposition behaviors on the Zn foil in different electrolytes. As shown in Figure 4e, the growth of dendrites can be seen in AqE after 4 min of deposition. In contrast, the surface of the plated Zn foil remained smooth and homogeneous even after 10 min (0.33 mAh cm^{-2}), demonstrating uniform Zn deposition in the WOE.

To unveil the mechanism behind the different electrodeposition behavior of the AqE and the WOE, different current densities (1, 2.5, 5, 7.5 mA cm^{-2}) were applied to deposit Zn with an areal capacity of 5 mAh cm^{-2} on Cu and Zn foils in Zn/Cu and Zn/Zn, respectively. Because the deposited crystalline structure with preferential facet growth is known to improve the performance of the electrodes, X-ray diffraction (XRD) analysis was employed to quantify the crystallinity of electrodeposited Zn from the two different electrolyte systems. Since the (111) peak of Cu overlaps with the (101) peak of Zn, the ratio between the (002) and (100) planes is more meaningful. As the current densities applied to the Zn/Cu half cells with the AqE were increased, the XRD patterns of Zn deposited Cu foil exhibited a slight increase in the peak intensity ratio of both $I(002)/I(100)$ and $I(002)/I(101)$ (Figure 4f; Figure S22a, Supporting Information). Compared to the AqE, the ratio of $I(002)/I(100)$ increased much more dramatically with the WOE as the applied current density was increased (Figure 4f,g; Figure S22b,c, Supporting Information). These results clearly demonstrate the preferable deposition of Zn (002) texture on Cu foil. Similarly, when employing Zn (instead of Cu) as a substrate, the ratio of $I(002)/I(100)$ also increased with applied current densities, demonstrating that Zn tends to deposit and expose the (002) facet on the Zn substrates when using the WOE (Figure S23a,b, Supporting Information). However, compared to the results obtained with Cu substrates, the changes in the ratios of $I(002)/I(100)$ and $I(002)/I(101)$ are not as pronounced when using Zn substrates due to diffraction from the non-electrodeposited Zn foil substrates (Figure S23c,d, Supporting Information). Compared to the WOE, the ratios of $I(002)/I(100)$ and $I(002)/I(101)$ were nearly constant at variable current densities in the AqE, suggesting a much less preferential facet for Zn electrodeposition in the AqE on Zn substrates, in agreement with the results obtained with Cu foil (Figure 4g). The preferential exposure of the (002) facet within WOE was also associated with a suppression of byproducts on the electrode surface. As depicted in Figure S24 (Supporting Information), XRD peaks belonging to byproducts can be observed on both Zn-deposited Cu and Zn foils cycled in the AqE, while the electrodes cycled in the WOE did not exhibit any byproducts. Moreover, the nucleation profiles of Zn deposition in Zn/Zn cells displayed larger nucleation overpotentials in the WOE as compared to the AqE at all current densities (Figure S25, Supporting Information). Considering the WOE exhibited a smaller contact angle with the Zn foil, this relative increase in nucleation overpotential could suggest that the WOE encourages more uniform deposition of smaller characteristic nuclei than AqE.

SEM and XRD characterizations were conducted to better understand the morphology evolution of the Zn anodes during prolonged cycling. Similar to the Zn deposited Zn foils with dendrites within the AqE, obvious Zn dendrites can be found on the cycled Zn anodes at different cycling numbers, indicating that nonuniform Zn plating occurred in the AqE (Figure S26, Supporting Information). In contrast for WOE, the (002) texture appeared after 20 cycles, which gradually became denser and more homogenous, resulting in a flat surface after 100 cycles (Figure S26, Supporting Information). The exposure of the (002) features within the WOE was confirmed by the XRD results, as the ratios of $I(002)/I(100)$ and $I(002)/I(101)$ increased along with the cycle numbers (Figure S27, Supporting Information). Therefore, the preferential exposure and accumulation of (002) textures facilitate the homogenous Zn deposition, even after prolonged cycling.

The preferential deposition of Zn in specific crystalline facets and its dependence on applied current density can likely be attributed to competition between thermodynamic and kinetic factors of electrodeposition and the influence of PC molecules.[76–78] Specifically, at low current density (<1 mA cm^{-2}), Zn deposition tends to thermodynamically occur at the facet with the lowest surface energy (i.e., (002) facet). With the increase of current density (>1 mA cm^{-2}), the kinetics-controlled deposition gradually replaces thermodynamics-governed crystalline growth. The high-index facets with high surface energy are activated (i.e., (100) and (101) facets), resulting in the simultaneous growth of all the facets at the same rate.[76] As such, the electrodeposition in AqE followed this behavior that all the Zn crystalline planes grow at a similar rate, and the ratios between different facets have barely changed with the increase of current density. In contrast, due to the possible adsorption of PC molecules varies on different planes, each crystalline facet could exhibit inconsistent deposition rates, which facilitates exposing the (002) facet. The increased current densities likely amplified the difference in the kinetics of each facet, eventually leading to more exposure of (002) texture with the increase in current density.

To understand the mechanism of exposing the (002) texture plane, the interactions between the Zn metal and the solvent molecules have been calculated with DFT, which compares the adsorption energy of water and PC at the electrode–electrolyte interface. The adsorption states of water and PC on the three low-energy facets of the Zn anode are shown in Figure 4h, which correspond to the adsorption energies of each state in Figure 4i. Compared with water, PC exhibits more negative (i.e., stronger) adsorption energy for all three facets, indicating that the organic PC molecules are more inclined to adsorb on the Zn surface than water, especially on the (002) facet. Due to the strong adsorption of PC on the (002) facet, which provides more steric

© 2023 Wiley-VCH GmbH

16163028, 0, Downloaded from https://onlinelibrary.wiley.com/doi/10.1002/adfm.202311271 by Northwestern University Libraries, Wiley Online Library on [15/12/2023]. See the Terms and Conditions (https://onlinelibrary.wiley.com/terms-and-conditions) on Wiley Online Library for rules of use; OA articles are governed by the applicable Creative Commons License

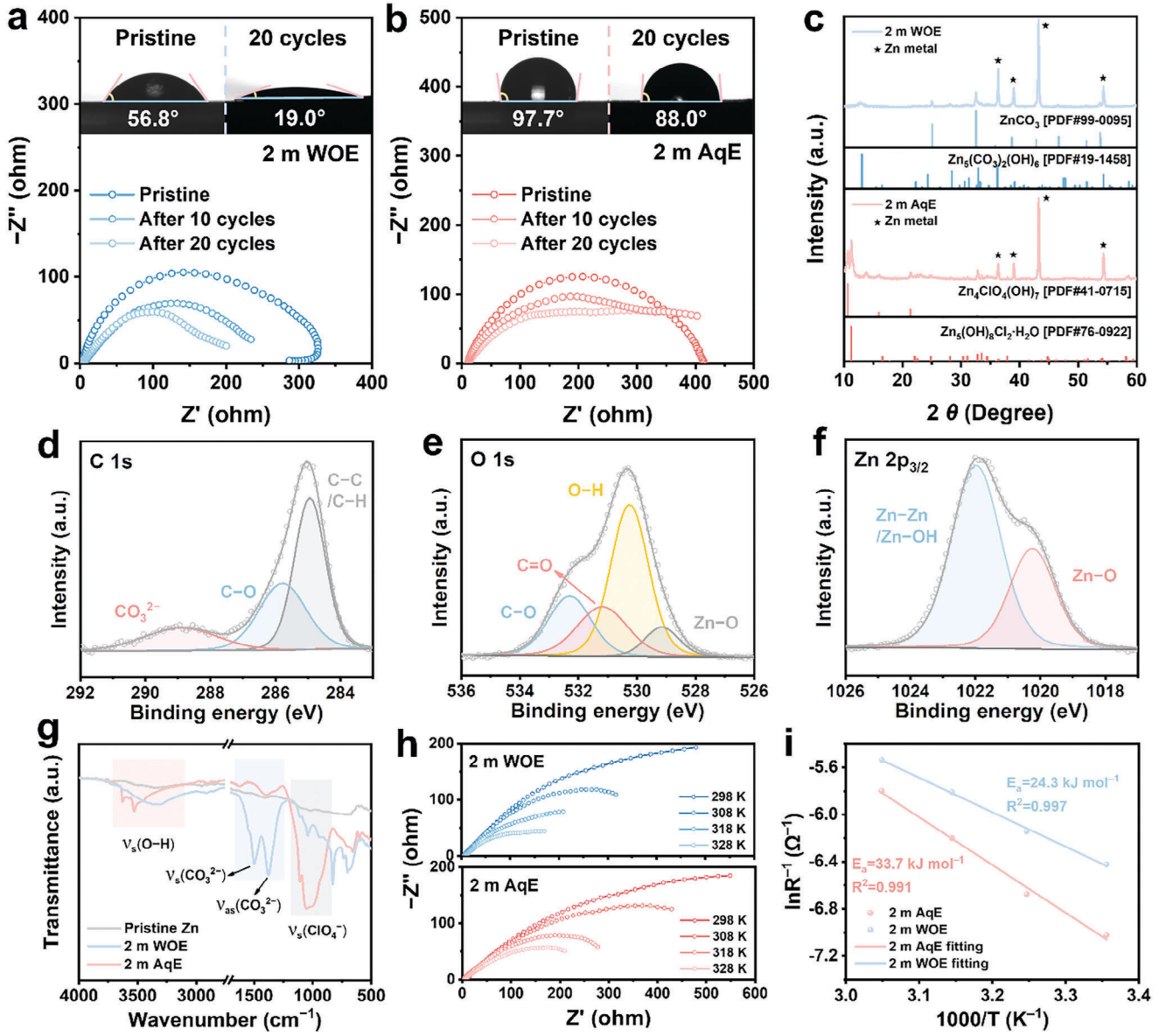

Figure 5. Characterization and structure of Zn anodes from Zn/Zn symmetric cells before and after cycling. Nyquist plots of Zn/Zn symmetric cells in a) WOE and b) AqE before and after cycling (the insets are contact angle results of Zn electrodes before and after 20 cycles). c) XRD patterns of Zn anodes after 20 cycles. d) C 1s, e) O 1s, and f) Zn 2p XPS spectra of the Zn anode after 20 cycles in the WOE. g) ATR-FTIR measurements of the pristine Zn foil and Zn anodes in both electrolytes after 20 cycles. h) Nyquist plots of Zn/Zn symmetric cells after 20 cycles, and i) corresponding activation energy data obtained from the Arrhenius equation and Nyquist plots.

hindrance of PC on the (002) plane, Zn^{2+} tends to nucleate and grow on the (101) and (100) texture planes rather than the (002) facet. In other words, the nucleation and growth rates on the (002) plane are lower than on the (101) and (100) planes, consequentially maintaining exposed (002) facets.[79,80] In addition, PC molecules adsorbed on the Zn surface further displace water from the interface and decrease the water decomposition. In contrast to WOE, water molecules exhibit similar adsorption energies on three main crystalline facets, which confirms that the preferential deposition of a certain facet hardly occurs in AqE, correlating to the XRD results of the AqE in Figure 4f,g.

2.4. Characterization of Electrolyte–Electrode Interface

Electrochemical impedance spectroscopy (EIS) of Zn/Zn symmetric cells was employed to evaluate the electrolyte–electrode interface and electrochemical performance of the Zn electrode. Between the initial and the 20th cycle, the Zn/Zn symmetric cell with the WOE exhibits a large decrease in charge transfer resistance from 323 to 176 Ω (**Figure 5**a). The contact angle of the WOE on the Zn surface decreased from 56.8° to 19.0° after cycling, illustrating enhanced wettability of the cycled Zn electrode. As compared to the WOE, the Zn/Zn cell with the AqE exhibits a similar decrease in impedance after 20 cycles

© 2023 Wiley-VCH GmbH

16163028, 0, Downloaded from https://onlinelibrary.wiley.com/doi/10.1002/adfm.202311271 by Northwestern University Libraries, Wiley Online Library on [15/12/2023]. See the Terms and Conditions (https://onlinelibrary.wiley.com/terms-and-conditions) on Wiley Online Library for rules of use; OA articles are governed by the applicable Creative Commons License

(418 to 263 Ω). However, the contact angle decreased to a much lesser extent (only ≈10° from 97.7° to 88.0 °) after cycling in the AqE (Figure 5b). These contrasting results from contact angle measurement may be attributed to modifications of the Zn surface in the WOE during electrochemical measurements, as $ZnCO_3$ and $Zn_5(CO_3)_2(OH)_8$ were detected on the Zn electrode cycled in WOE via XRD (Figure 5c). In the AqE, XRD revealed different crystalline hydroxide species (e.g., $Zn_4ClO_4(OH)_7$ and $Zn_5(OH)_8Cl_2{\bullet}H_2O$), commonly reported as byproducts from water decomposition and that accelerate parasitic reactions and Zn dendrites formations to impact performance negatively.[81–83] In contrast, the carbonate species generated in the WOE (e.g., $ZnCO_3$ and $Zn_5(CO_3)_2(OH)_8$) instead comprise a protective SEI layer that regulates Zn deposition and prevents unfavorable side reactions.[25,84,85]

X-ray photoelectron spectroscopy (XPS) analyses of the cycled Zn electrodes were conducted to understand the composition of the SEI layer. Survey scans revealed the presence of C, O, Zn, and Cl species on the surface (Figure S28, Supporting Information). As for the Zn cycled in the WOE, in the C 1s spectrum, the main peak of the C—C signal may be attributed to the atmospheric carbon adsorbed on the Zn surface (Figure 5d). The component near 288.7 eV in the C 1s spectrum can be assigned to CO_3^{2-} motifs in the interphase (as detected by XRD). Likewise, the C═O signal in the O 1s spectrum also arises from the existence of CO_3^{2-} species originating from the decomposition of adsorbed PC molecules during cycling (Figure 5e). Furthermore, Zn—OH and Zn—O features observed in the Zn 2p spectrum, with corresponding O—H and Zn—O lattice signals in the O 1s spectrum, confirm the formation of $Zn_5(CO_3)_2(OH)_8$ (Figure 5f). However, though XPS of the Zn anode cycled in the WOE lacks Cl species, the Cl 2p spectrum of AqE exhibits significant signals from ClO_4^- and Cl^-, corresponding to the $Zn_4ClO_4(OH)_7$ and $Zn_5(OH)_8Cl_2{\bullet}H_2O$ revealed by XRD (Figure S29, Supporting Information). Further measurement of the Zn surfaces was conducted via ATR-FTIR after cycling in the AqE and the WOE. The FTIR spectrum of AqE contains obvious features from ClO_4^- and O—H vibrations stemming from the $Zn_4ClO_4(OH)_7$ byproduct (Figure 5g). In contrast, intense peaks near 1500 cm^{-1} assigned to a stretching vibration of CO_3^{2-} were observed for the Zn electrode cycled in the WOE, confirming the formation of CO_3^{2-} species on the Zn anode surface.[86,87] Further, EDX results of the Zn surface after cycling illustrate the even distribution of C on the Zn surface cycled in the WOE, and the formation of nonuniform nanoflower structures of Cl-containing byproducts for the Zn electrode cycled in the AqE (Figure S30, Supporting Information). Differences in the species comprising the inorganic SEI layer can significantly impact the interfacial reaction kinetics by modulating charge transfer at the electrode–electrolyte interface.[88–91] To evaluate the interfacial process, the activation energy of charge transfer for the cycled anode was calculated based on the EIS results and the Arrhenius equation (Figure 5h; FIgure S31, Supporting Information). The calculation results show a smaller activation energy in the WOE than the AqE (Figure 5i), illustrating that the SEI layer can efficiently facilitate the charge transfer process, which is favorable for Zn deposition. Furthermore, the inorganic SEI layer also limits the electron transfer between electrolyte and Zn anode due to their electronically insulating properties, effectively suppressing the water decomposition and kinetically enlarging the electrochemical stability window during operation.[85]

2.5. Investigation of Zn-Vanadium Batteries

Full cells with Zn anodes and $Na_{0.33}V_2O_5$ (NaVO) cathodes were assembled to evaluate the utility of the WOE in zinc-ion batteries. The successful hydrothermally synthesized NaVO nanobelts based on previous literature were confirmed by the XRD pattern and SEM images (Figure S32, Supporting Information).[92] Initially, the CV measurements were conducted to unveil the energy storage mechanism in the NaVO/Zn full cells within different electrolytes. As demonstrated in Figure S33a (Supporting Information), the CV curves of NaVO/Zn batteries exhibit similar shapes. The peak shift toward lower potential in the WOE during the reduction scan can be ascribed to the change of reaction kinetics due to stronger solvation in the PC-modified electrolyte.[93,94] Notably, although the peak shift in the XRD patterns represents the intercalation of charges (Figure S34, Supporting Information), compared with the CV curve in the AqE, no additional peak appeared in the curve of WOE. This result indicates that only Zn^{2+} and H^+ intercalated into the layered structure, while PC molecules did not participate in energy storage.[83,95] Moreover, the CV curves in the initial five cycles demonstrate that the NaVO/Zn batteries cycled in both electrolytes with high reversibility (Figure S33b,c, Supporting Information). Owing to the stability of the Zn anode and NaVO cathode, the NaVO/Zn battery cycled stably for at least 100 cycles at 0.1 A g^{-1} in the WOE, while the full cell in the AqE delivered a poor durability of 15% retention after 100 cycles (**Figure 6**a). Moreover, the NaVO/Zn battery in WOE exhibits favorable rate performance and kinetics. The recovered capacity (285 mAh g^{-1}) at 0.1 A g^{-1} after high current densities maintains almost the same value (288 mAh g^{-1}) as the initial cycling at 0.1 A g^{-1} (Figure 6b). In contrast, the NaVO/Zn battery with AqE only achieved a 70% capacity recovery after high-current cycling. In addition, the galvanostatic charge/discharge (GCD) curves at different current densities indicate a larger overpotential in AqE (0.1 V) than in WOE (0.07 V), which results in superior capacity and reaction kinetics in WOE (Figure 6c; FIgure S35, Supporting Information). The more obvious polarization in AqE is likely due to the accumulation of byproducts and side reactions on the electrodes. Upon increasing the current density to 2 A g^{-1}, a capacity drop was observed for the NaVO/Zn battery with AqE during cycling (Figure 6d). However, in WOE, no capacity fading was observed, but a capacity activation process appeared until cycling 800 cycles. The capacity increase can be attributed to the exfoliation of the cathode, which increased the surface area (Figure S36, Supporting Information) and provided more accessible sites for charge transfer and energy storage.

To understand the difference in the cycling performance between the two electrolytes, initially, the surfaces of Zn anodes in NaVO/Zn batteries after cycling were also characterized. Zn dendrites and byproducts were found on the surface of the cycled Zn anode in the AqE, while the anode in the WOE was found to exhibit uniform Zn deposition with preferential (002) morphology (Figure 6e). Additionally, the XRD pattern of the Zn anode cycled in the WOE not only confirms the formation of a large amount

© 2023 Wiley-VCH GmbH

16163028, 0, Downloaded from https://onlinelibrary.wiley.com/doi/10.1002/adfm.202311271 by Northwestern University Libraries, Wiley Online Library on [15/12/2023]. See the Terms and Conditions (https://onlinelibrary.wiley.com/terms-and-conditions) on Wiley Online Library for rules of use; OA articles are governed by the applicable Creative Commons License

16163028, 0, Downloaded from https://onlinelibrary.wiley.com/doi/10.1002/adfm.202311271 by Northwestern University Libraries, Wiley Online Library on [15/12/2023]. See the Terms and Conditions (https://onlinelibrary.wiley.com/terms-and-conditions) on Wiley Online Library for rules of use; OA articles are governed by the applicable Creative Commons License

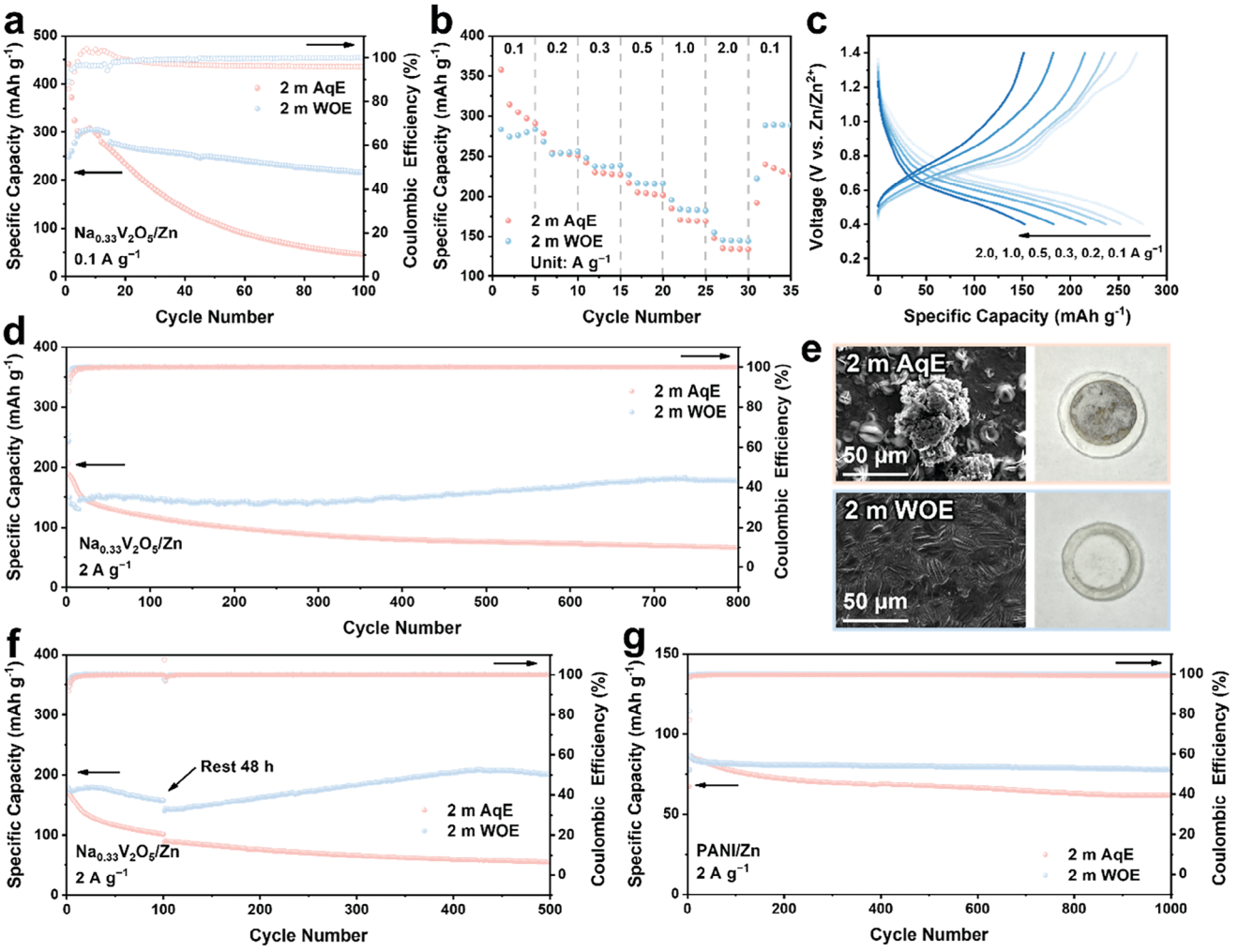

Figure 6. Electrochemical performance of NaVO/Zn and PANI/Zn full cells. a) Cycling performance of NaVO/Zn batteries at 0.1 A g^{-1} in both electrolytes. b) Rate performance of NaVO/Zn batteries under current densities from 0.1 to 2 A g^{-1} in both electrolytes. c) Corresponding GCD curves of the battery within the WOE. d) Long-time cycling performance of NaVO/Zn batteries at 2 A g^{-1}, and e) corresponding SEM images of Zn anodes and digital photos of separators after cycling. f) Cycling performance of NaVO/Zn batteries at 2 A g^{-1} with a rest for 48 h at the 100th cycle. g) Cycling performance of PANI/Zn batteries at 2 A g^{-1}.

of (002) facet, corresponding to the SEM results, but also reveals the formation of an inorganic SEI layer on the electrode surface (Figure S37, Supporting Information). Fewer byproducts, more uniform Zn deposition, and the coating of the SEI layer on the Zn anode surface confirmed the reduced electrolyte decomposition and high Zn^{2+} utilization in the WOE, contributing to capacity retention.[49] In contrast, preferential Zn deposition was not observed on the Zn anode cycled in the AqE; instead, XRD peaks corresponding to the NaVO cathode materials indicated the presence of NaVO on the Zn anode surface, which was further confirmed by the EDX results (Figure S38, Supporting Information). This unexpected appearance of cathode materials on the anode side is mainly caused by the dissolution of the cathode into the electrolyte and the following shuttle effect.[96] To visualize the cathode dissolution, the separators were removed from full cells after cycling 800 cycles in AqE and WOE (Figure 6e). At the center of the separator in the AqE, a dark brown region due to the dissolution of the cathode can be observed. However, the separator from the WOE remained pristine, suggesting that the confined water activity in the WOE prevented the dissolution of NaVO. For further investigation, NaVO cathodes were soaked in different electrolytes for several days to assess cathode dissolution (Figure S39, Supporting Information). Due to the lower water content and restricted water activity, the color of the OE and the WOE hardly changed after soaking for 6 days. In contrast, a stark color change for the AqE began after two days of soaking and continued over 6 days. Such a color change of the electrolyte can be ascribed to the dissolution of vanadate-based species into the electrolyte.[95] The above results demonstrate that the WOE efficiently suppresses the dissolution of NaVO to aid in the cycling stability of full cells. (Figure S40, Supporting Information)

Full-cell zinc-ion batteries employing NaVO are commonly susceptible to parasitic self-discharge related to corrosion and side reactions occurring on the Zn anode surface. In order to investigate the impact of the electrolyte on self-discharge, the electrochemical tests at 2 A g^{-1} were stopped after 100 cycles, and

 © 2023 Wiley-VCH GmbH

the fully-charged batteries were rested for 48 h before continued cycling. The cycling performance in the AqE provides a similar trend to normal cycling, where continuous capacity fading was observed after resting (Figure 6f). However, although there is evidence of self-discharge after resting at 100% SOC in the WOE, a capacity-activation process similar to the performance during constant cycling was observed. The open circuit voltage profile of fully charged NaVO/Zn batteries in the WOE displays a capacity retention of 90.3%, in comparison to 86.1% for the AqE (Figure S40, Supporting Information). The capacity decay in the AqE is due to the severe dissolution of the cathode and parasitic reactions on the anode. Although NaVO/Zn batteries within WOE exhibit promising cycling performance, the N/P ratio in the NaVO/Zn batteries is 123, indicating that the utilization of the Zn anode is less than 1%. Therefore, it is necessary to cycle the NaVO/Zn batteries under lean-Zn conditions. The Cu foils with 2.3 mAh cm^{-2} deposited Zn metal served as the anodes, where the N/P ratio is 5. As shown in Figure S41 (Supporting Information), the NaVO/Zn battery within the WOE still maintains stable cycling over 800 cycles with an average capacity of 150 mAh g^{-1}, which is similar to the NaVO/Zn battery with excess Zn. However, the full cell employing the AqE displays a continuous capacity decay. These results demonstrate the practical application of WOE under lean-Zn conditions. In general, applying the WOE in Zn-vanadium batteries is a promising strategy for high-stability and high-performance zinc-ion batteries.

In addition to using NaVO as the cathode material, the organic polyaniline (PANI) was applied as the cathode to evaluate the practicability of the WOE. Figure 6g shows stable cycling of PANI/Zn battery within the WOE over 1000 cycles with a capacity retention of 90%. In contrast, a more significant capacity decay was observed in the PANI/Zn battery within the AqE, which only maintained a capacity retention of 70%, demonstrating that the WOE is suitable for the zinc-ion batteries with organic cathodes.

2.6. Electrochemical Performance across a Wide Temperature Range

The high freezing point (around 0°C) of water restricts the Zn^{2+} transport and ionic conductivity in the electrolytes, which limits the battery operation under subzero temperatures. In contrast, PC exhibits a wide temperature range from −48.8 to 242 °C, and the mixture of PC and water inherits the wide operating temperature range.[97] Meanwhile, as a strong chaotropic salt, $Zn(ClO_4)_2$ can effectively break the original H bonds of water molecules to provide anti-freezing properties with the electrolytes.[42,98] With the aid of the synergistic effect of PC and $Zn(ClO_4)_2$ salt, the 2 m WOE exhibits promising anti-freezing properties under −20 °C and remains in the liquid phase without ice formation, which may be attributed to the breaking of H-bonded water networks by PC and $Zn(ClO_4)_2$ molecules (**Figure 7**a). However, AqE freezes at −20 °C, confirming the instability of aqueous electrolytes at subzero temperatures. The differential scanning calorimetry (DSC) results shown in Figure S42 (Supporting Information) support that the instant vitrification temperature of AqE is only −38.3 °C, while the absence of the peak in the WOE within the selected temperature range means the freezing point is below −70 °C. In comparison to AqE, the hydrogen bonds between PC and water in the WOE are more effective and have a great impact on the anti-freezing properties at lower temperatures. While $Zn(ClO_4)_2$ chaotropic salt can help to decrease the freezing point, its primary function is to stabilize and homogenize the WOE under low temperatures, preventing any phase separation. Further, the ionic conductivities at different temperatures were collected via EIS (Figure S43, Supporting Information). As shown in Figure 7b, the WOE remains in the liquid regime of ion transport over all investigated temperatures. Even at −20 °C, the WOE maintains an appreciable ionic conductivity of 21.4 mS cm^{-1}. In contrast, the AqE crosses into the sluggish solid transport regime at subzero temperatures with a dramatic decrease in ionic conductivity at −20 °C to ≈1.0 mS cm^{-1}. Further, the activation energies (E_a) of ion conduction in the AqE and the WOE were calculated based on the Arrhenius relationship between ionic conductivity and temperature. As depicted in Figure 7c, the results of the WOE maintain a constant slope at all the temperatures with a calculated activation energy of 6.88 kJ mol^{-1}, indicating fast ion transport even at subzero temperatures. In contrast, an obvious transition can be observed in the AqE at 0 °C. The activation energy of 5.74 kJ mol^{-1} at above-zero temperatures implies desirable ionic transport. The lower activation energy of the AqE compared with the WOE corresponds to the higher ionic conductivity of the AqE mentioned previously. However, the activation energy of 82.97 kJ mol^{-1} at subzero temperatures confirms the significantly reduced ionic diffusion due to the solidification of the AqE. These superior physicochemical properties of the WOE facilitate the performance of zinc-ion batteries under low temperatures.

The characteristics of Zn plating/stripping performance in the WOE over a wide temperature range (i.e., −20 to 50°C) were investigated in Zn/Cu half cells. The Zn/Cu cell with the WOE was able to achieve stable Zn plating/stripping at −20°C for over 2000 cycles with an average CE of 97.5%. In contrast, the obvious fluctuation and instability of CE in AqE, followed by a significant failure at around 200 cycles, reflect the insufficient Zn^{2+} transport in frozen AqE (Figure 7d). On the other hand, at a temperature as high as 50 °C, the WOE maintains an average CE of 98.7% over 2000 stable cycles. However, in the AqE, the CE decayed dramatically after 150 cycles, likely due to the more facile kinetics of parasitic reactions at increased temperature (Figure 7e). In addition, because of the highly reversible Zn plating/stripping in the WOE, Zn/Zn symmetric cells in the WOE perform well under wide temperature ranges. The Zn/Zn symmetric cell in the WOE cycled for 400 h under −20°C without significant failure or a short circuit (Figure 7f). Compared with the Zn/Zn cell cycling at room temperature, the increased overpotential below −20 °C is likely attributed to a more difficult desolvation process at low temperatures, thermodynamically increasing the energy barrier for the desolvation process.[99] Stable cycling performance was observed with the WOE at 50 °C (Figure 7g). However, with the AqE, the Zn/Zn symmetric cells exhibit short circuits and failure at both −20 and 50 °C, most likely as a result of uncontrollable Zn dendrite formation and water dissociation-related side reactions, respectively, during cycling.

NaVO/Zn full-cell batteries were assembled to evaluate the cycling stability across a wide temperature range. Figure S44a (Supporting Information) shows that the NaVO/Zn battery in the WOE can cycle with a specific capacity of 30 mAh g^{-1} over 3000 cycles stably after a 500-cycle slight capacity decay at −20 °C.

© 2023 Wiley-VCH GmbH

16163028, 0, Downloaded from https://onlinelibrary.wiley.com/doi/10.1002/adfm.202311271 by Northwestern University Libraries, Wiley Online Library on [15/12/2023]. See the Terms and Conditions (https://onlinelibrary.wiley.com/terms-and-conditions) on Wiley Online Library for rules of use; OA articles are governed by the applicable Creative Commons License

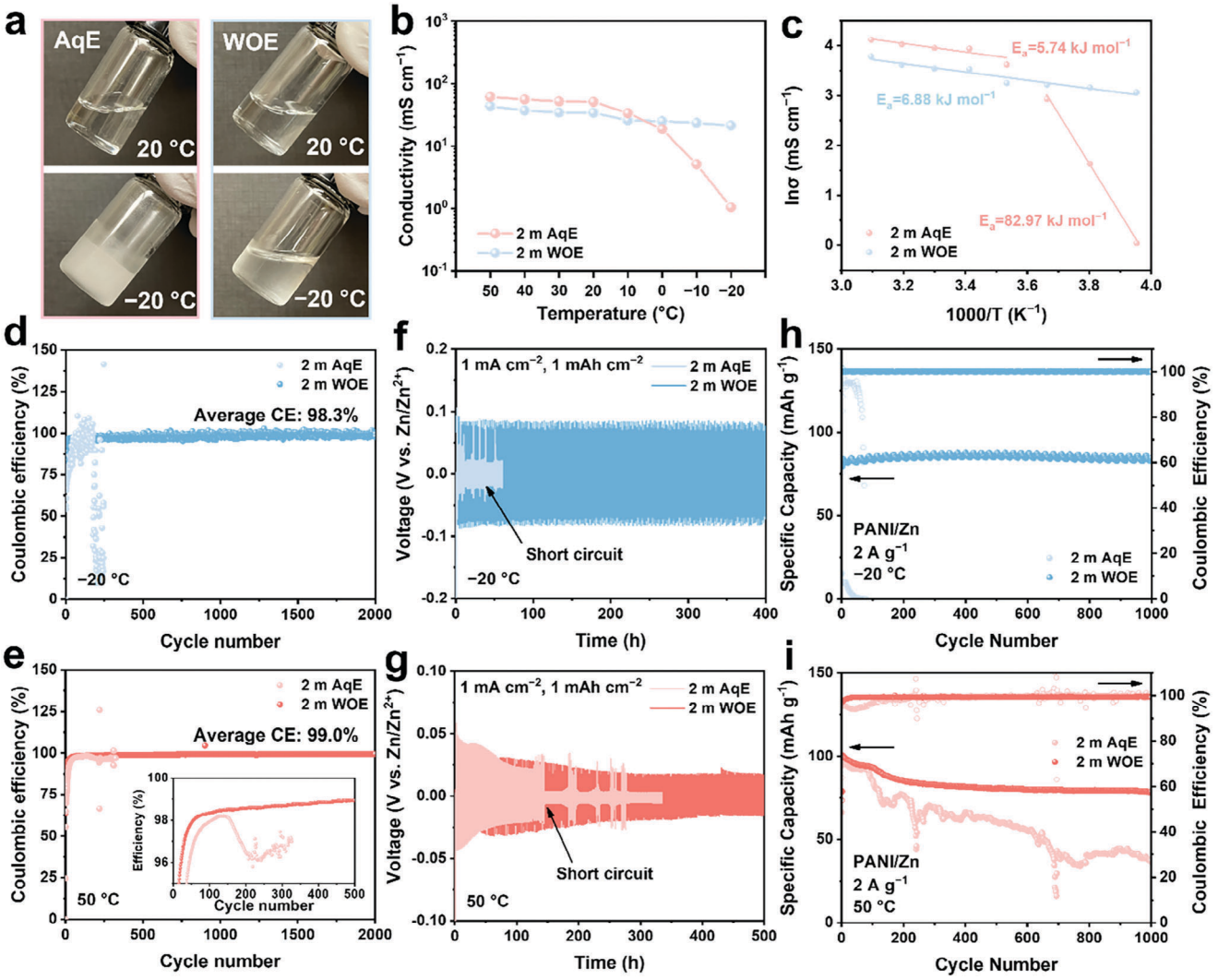

Figure 7. Characterization and electrochemical performance of different electrolytes under a temperature range from −20 to 50 °C. a) Digital photos of AqE and WOE under 20°C and −20°C. b) Ionic conductivity of both electrolytes from 50 to −20 °C, and (c) corresponding Arrhenius plot for calculating conductive activation energy. Coulombic efficiencies of Zn/Cu half cells under d) −20 and e) 50°C. Cycling performance of Zn/Zn symmetric cells at 1 mA cm^{-2} to a capacity of 1 mAh cm^{-2} under (f) −20 and g) 50°C. Cycling performance of PANI/Zn full cells under 2 A g^{-1} at h) −20 and i) 50 °C.

Moreover, an average CE of nearly 100% illustrates the highly reversible (de)intercalation of Zn^{2+} in the cathode and Zn plating/stripping on the anode. However, due to the low ionic conductivity in the frozen AqE, the NaVO/Zn exhibits negligible capacity and a low CE under identical conditions. Clearly, the AqE cannot be employed in zinc-ion batteries at subzero temperatures. Additionally, the impact of both electrolytes on the performance of zinc-ion batteries at 50 °C was assessed. At the high temperature, the dissolution equilibrium of cathode materials would be influenced, which may accelerate the dissolution of the cathode in the electrolyte. As shown in Figure S44b (Supporting Information), the NaVO/Zn battery with the AqE exhibits a continuous capacity decay for 100 cycles under 50 °C, while the WOE maintains a capacity retention of 91% after 100 cycles. The drastic capacity fade in the AqE can be attributed to the cathode dissolution, which worsens at high temperatures. As Figure S45a,b (Supporting Information) suggested, noticeable brown deposits are visible on the separator and on the Zn anode due to the shuttle effect of the cathode materials dissolved in the electrolyte and transported to the anode, which deteriorates the performance of zinc-ion batteries.[100,101] In contrast, both the separator and zinc anode in the WOE remain pristine and free of vanadate deposits, indicating the stability of the cathode in the WOE at high temperatures (Figure S45c,d, Supporting Information).

Although the cycling performance of NaVO/Zn batteries was found to be more sustainable in the WOE than the AqE, the low specific capacity at −20 °C and short lifespan at 50 °C restrict their application under extreme temperatures. Unlike NaVO, which owns an intercalation mechanism for energy storage, the organic PANI involves surface redox reactions, which are not sensitive to temperature change.[102] Therefore, PANI/Zn batteries were cycled under different temperatures in both AqE and WOE. As depicted in Figure 7h, PANI/Zn battery within the WOE can cycle stably over 1000 cycles with a higher capacity (80 mAh g^{-1})

© 2023 Wiley-VCH GmbH

16163028, 0, Downloaded from https://onlinelibrary.wiley.com/doi/10.1002/adfm.202311271 by Northwestern University Libraries, Wiley Online Library on [15/12/2023]. See the Terms and Conditions (https://onlinelibrary.wiley.com/terms-and-conditions) on Wiley Online Library for rules of use; OA articles are governed by the applicable Creative Commons License

16163028, 0, Downloaded from https://onlinelibrary.wiley.com/doi/10.1002/adfm.202311271 by Northwestern University Libraries, Wiley Online Library on [15/12/2023]. See the Terms and Conditions (https://onlinelibrary.wiley.com/terms-and-conditions) on Wiley Online Library for rules of use; OA articles are governed by the applicable Creative Commons License

than NaVO/Zn battery (30 mAh g^{-1}) at −20 °C. In contrast, the PANI/Zn battery within the AqE exhibits a drastic capacity decay in the initial 100 cycles with low CE, similar to the NaVO/Zn battery within the AqE. At 50 °C, PANI/Zn battery performs higher stability over 1000 cycles than NaVO/Zn with a capacity of 90 mAh g^{-1}, while the unsustainable cycling with low CE appears in PANI/Zn battery cycled in AqE (Figure 7i). The above results confirm the promising potential of the WOE for practical applications under extreme conditions.

3. Conclusion

In summary, we designed a non-flammable "water-in-organic" electrolyte by adding water as a co-solvent into a PC-based organic electrolyte. To create a homogenous solution, the $Zn(ClO_4)_2$ chaotropic salt was utilized as a solubilizer to combine two immiscible liquids (i.e., water and PC). Adding water to the PC electrolytes improved safety, decreased viscosity, and increased ionic conductivity without sacrificing the electrochemical stability window. Spectroscopic characterizations and quantum chemical calculations supported that a strong interaction between PC and water restricted the water activity and that the PC molecules excluded the water from the inner Zn^{2+} solvation sheath. Together, these effects minimized side reactions caused by water decomposition. Additionally, the adsorption of PC molecules on the Zn anode surface encouraged exposure of Zn (002) facets to suppress parasitic reactions and dendrites. The decomposition of adsorbed PC molecules formed a robust and protective inorganic SEI layer, providing enhanced charge transfer compared with conventional organic SEI. As a result, this "water-in-organic" electrolyte facilitated reversible Zn plating/stripping for over 1000 h in symmetric cells and sustainable cycling for over 800 cycles in zinc-vanadate full-cell batteries. Moreover, the modulated H-bonding intermolecular interactions between water and PC enabled the "water-in-organic" electrolyte to operate across a wide temperature range from −20 to 50 °C. Corresponding highly reversible Zn plating/stripping for 2000 h and the excellent performance of full cell cycling over 3000 cycles demonstrate the utility of this "water-in-organic" electrolyte working under extreme conditions. In summary, the "water-in-organic" electrolyte not only manipulates the electrode-electrolyte interface via controlling surface adsorption and interfacial reactions but also restricts water activity by regulating electrolyte structure, providing superior reversibility and stability with zinc-ion batteries. Hybridizing existing organic electrolytes with a sufficient amount of water to inhibit flammability and a proper chaotropic salt as a solubilizer efficiently combines the advantages of organic and aqueous electrolytes and represents a new strategy to enable future safe, low-cost, and high-performance zinc-ion batteries.

Supporting Information

Supporting Information is available from the Wiley Online Library or from the author.

Acknowledgements

The authors gratefully acknowledge the Welch Foundation for their generous support through Grant No.'s F-1436 (C.B.M.) and F-1841 (G.H.). This research was partially supported by the National Science Foundation through the Center for Dynamics and Control of Materials: an NSF MRSEC under Cooperative Agreement No. DMR-1720595.

Conflict of Interest

The authors declare no conflict of interest.

Data Availability Statement

The data that support the findings of this study are available in the supplementary material of this article.

Keywords

chaotropic salt, enlarged electrochemical window, solid electrolyte interphase, wide temperature range, zinc-ion batteries, Zn (002) deposition

Received: September 17, 2023
Revised: October 29, 2023
Published online:

[1] S. K. Heiskanen, J. Kim, B. L. Lucht, *Joule* **2019**, *3*, 2322.
[2] Q. Wang, L. Jiang, Y. Yu, J. Sun, *Nano Energy* **2019**, *55*, 93.
[3] A. M. Haregewoin, A. S. Wotango, B.-J. Hwang, *Energy Environ. Sci.* **2016**, *9*, 1955.
[4] M. Li, J. Lu, Z. Chen, K. Amine, *Adv. Mater.* **2018**, *30*, 1800561.
[5] J. Deng, C. Bae, A. Denlinger, T. Miller, *Joule* **2020**, *4*, 511.
[6] L. E. Blanc, D. Kundu, L. F. Nazar, *Joule* **2020**, *4*, 771.
[7] G. Fang, J. Zhou, A. Pan, S. Liang, *ACS Energy Lett.* **2018**, *3*, 2480.
[8] N. Zhang, X. Chen, M. Yu, Z. Niu, F. Cheng, J. Chen, *Chem. Soc. Rev.* **2020**, *49*, 4203.
[9] T. Zhang, Y. Tang, S. Guo, X. Cao, A. Pan, G. Fang, J. Zhou, S. Liang, *Energy Environ. Sci.* **2020**, *13*, 4625.
[10] J. Xu, X. Ji, J. Zhang, C. Yang, P. Wang, S. Liu, K. Ludwig, F. Chen, P. Kofinas, C. Wang, *Nat. Energy* **2022**, *7*, 186.
[11] H. Zhang, Xu Liu, H. Li, I. Hasa, S. Passerini, *Angew. Chem., Int. Ed. Engl.* **2021**, *60*, 598.
[12] M. Pasta, C. D. Wessells, R. A. Huggins, Y. Cui, *Nat. Commun.* **2012**, *3*, 1149.
[13] Y. Xu, X. Zhou, Z. Chen, Y. Hou, Y. You, J. Lu, *Mater. Today* **2023**, *66*, 339.
[14] X. Gao, Y. Dai, C. Zhang, Y. Zhang, W. Zong, W. Zhang, R. Chen, J. Zhu, X. Hu, M. Wang, R. Chen, Z. Du, F. Guo, H. Dong, Y. Liu, H. He, S. Zhao, F. Zhao, J. Li, I P. Parkin, C. J. Carmalt, G. He, *Angew. Chem., Int. Ed. Engl.* **2023**, *62*, 202300608.
[15] Y. Wang, T. Wang, S. Bu, J. Zhu, Y. Wang, R. Zhang, H. Hong, W. Zhang, J. Fan, C. Zhi, *Nat. Commun.* **2023**, *14*, 1828.
[16] V. Verma, S. Kumar, W. Manalastas, M. Srinivasan, *ACS Energy Lett.* **2021**, *6*, 1773.
[17] A. Bayaguud, X. Luo, Y. Fu, C. Zhu, *ACS Energy Lett.* **2020**, *5*, 3012.
[18] W. Yang, Y. Yang, H. Yang, H. Zhou, *ACS Energy Lett.* **2022**, *7*, 2515.
[19] W. Wang, C. Yang, X. Chi, J. Liu, B. Wen, Y. Liu, *Energy Stor. Mater.* **2022**, *53*, 774.
[20] Y. Wang, Z. Wang, W. K. Pang, W. Lie, J. A. Yuwono, G. Liang, S. Liu, A. M. D' Angelo, J. Deng, Y. Fan, K. Davey, B. Li, Z. Guo, *Nat. Commun.* **2023**, *14*, 2720.
[21] S. Liu, J. Mao, W. K. Pang, J. Vongsvivut, X. Zeng, L. Thomsen, Y. Wang, J. Liu, D. Li, Z. Guo, *Adv. Funct. Mater.* **2021**, *31*, 2104281.

 © 2023 Wiley-VCH GmbH

[22] H. Ren, S. Li, B. Wang, Y. Zhang, T. Wang, Q. Lv, X. Zhang, L. Wang, X. Han, F. Jin, C. Bao, P. Yan, N. Zhang, D. Wang, T. Cheng, H. Liu, S. Dou, *Adv. Mater.* **2023**, *35*, 2208237.
[23] D. E. Ciurduc, C. De La Cruz, N. Patil, A. Mavrandonakis, R. Marcilla, *Energy Stor. Mater.* **2022**, *53*, 532.
[24] D. E. Ciurduc, C. De La Cruz, N. Patil, A. Mavrandonakis, R. Marcilla, *Mater. Today Energy* **2023**, *36*, 101339.
[25] C. Li, R. Kingsbury, A. S. Thind, A. Shyamsunder, T. T. Fister, R. F. Klie, K. A. Persson, L. F. Nazar, *Nat. Commun.* **2023**, *14*, 3067.
[26] W. Yang, X. Du, J. Zhao, Z. Chen, J. Li, J. Xie, Y. Zhang, Z. Cui, Q. Kong, Z. Zhao, C. Wang, Q. Zhang, G. Cui, *Joule* **2020**, *4*, 1557.
[27] R. Chen, C. Zhang, J. Li, Z. Du, F. Guo, W. Zhang, Y. Dai, W. Zong, X. Gao, J. Zhu, Y. Zhao, X. Wang, G. He, *Energy Environ. Sci.* **2023**, *16*, 2540.
[28] X. Lin, G. Zhou, M. J. Robson, J. Yu, S. C. T. Kwok, F. Ciucci, *Adv. Funct. Mater.* **2022**, *32*, 2109322.
[29] Z. Liu, R. Wang, Q. Ma, J. Wan, S. Zhang, L. Zhang, H. Li, Q. Luo, J. Wu, T. Zhou, J. Mao, L. Zhang, C. Zhang, Z. Guo, *Adv. Funct. Mater.* **2023**, 2214538.
[30] B. Kakoty, R. Vengarathody, S. Mukherji, V. Ahuja, A. Joseph, C. Narayana, S. Balasubramanian, P. Senguttuvan, *J. Mater. Chem. A* **2022**, *10*, 12597.
[31] Z. Li, Y. Liao, Y. Wang, J. Cong, H. Ji, Z. Huang, Y. Huang, *Energy Stor. Mater.* **2023**, *56*, 174.
[32] Z. Chen, T. Liu, Z. Zhao, Z. Zhang, X. Han, P. Han, J. Li, J. Wang, J. Li, S. Huang, X. Zhou, J. Zhao, G. Cui, *J. Power Sources* **2020**, *457*, 227994.
[33] N. Zhang, Y. Dong, Y. Wang, Y. Wang, J. Li, J. Xu, Y. Liu, L. Jiao, F. Cheng, *ACS Appl. Mater. Interfaces* **2019**, *11*, 32978.
[34] Z. Chen, Y. Tang, X. Du, B. Chen, G. Lu, X. Han, Y. Zhang, W. Yang, P. Han, J. Zhao, G. Cui, *Angew. Chem., Int. Ed. Engl.* **2020**, *59*, 21769.
[35] Y. Lv, Y. Xiao, L. Ma, C. Zhi, S. Chen, *Adv. Mater.* **2022**, *34*, 2106409.
[36] T. A. Nigatu, H. K. Bezabh, B. W. Taklu, B. W. Olbasa, Y.-T Weng, S.-H. Wu, W.-N. Su, C.-C. Yang, B. J. Hwang, *J. Power Sources* **2021**, *511*, 230413.
[37] W. Deng, Z. Xu, X. Wang, *Energy Stor. Mater.* **2022**, *52*, 52.
[38] L. Geng, J. Meng, X. Wang, C. Han, K. Han, Z. Xiao, M. Huang, P. Xu, L. Zhang, L. Zhou, L. Mai, *Angew. Chem., Int. Ed. Engl.* **2022**, *61*, 202206717.
[39] S. Huang, L. Hou, T. Li, Y. Jiao, P. Wu, *Adv. Mater.* **2022**, *34*, 2110140.
[40] Y. Zhang, P. Cremer, *Curr. Opin. Chem. Biol.* **2006**, *10*, 658.
[41] S. Wu, M. Hua, Y. Alsaid, Y. Du, Y. Ma, Y. Zhao, C.-Y. Lo, C. Wang, D. Wu, B. Yao, J. Strzalka, H. Zhou, X. Zhu, X. He, *Adv. Mater.* **2021**, *33*, 2007829.
[42] G. Yang, J. Huang, X. Wan, B. Liu, Y. Zhu, J. Wang, O. Fontaine, S. Luo, P. Hiralal, Y. Guo, H. Zhou, *EcoMat* **2022**, *4*, e12165.
[43] P. Lo Nostro, B. W. Ninham, *Chem. Rev.* **2012**, *112*, 2286.
[44] Z. Xu, H. Li, Y. Liu, K. Wang, H. Wang, M. Ge, J. Xie, J. Li, Z. Wen, H. Pan, S. Qu, J. Liu, Y. Zhang, Y. Tang, S. Chen, *Mater. Horiz.* **2023**.
[45] J. Feng, X. Li, X. Cui, H. Zhao, K. Xi, S. Ding, *Adv. Energy Mater.* **2023**, *13*, 2204092.
[46] H. Zhang, Y. Zhong, J. Li, Y. Liao, J. Zeng, Y. Shen, L. Yuan, Z. Li, Y. Huang, *Adv. Energy Mater.* **2023**, *13*, 2203254.
[47] J. Cao, D. Zhang, C. Gu, X. Wang, S. Wang, X. Zhang, J. Qin, Z.-S. Wu, *Adv. Energy Mater.* **2021**, *11*, 2101299.
[48] T. Wei, Y. Ren, Y. Wang, L. Mo, Z. Li, H. Zhang, L. Hu, G. Cao, *ACS Nano* **2023**, *17*, 3765.
[49] M. Zhou, S. Guo, J. Li, X. Luo, Z. Liu, T. Zhang, X. Cao, M. Long, B. Lu, A. Pan, G. Fang, J. Zhou, S. Liang, *Adv. Mater.* **2021**, *33*, 2100187.
[50] Z. Zhao, R. Wang, C. Peng, W. Chen, T. Wu, Bo Hu, W. Weng, Y. Yao, J. Zeng, Z. Chen, P. Liu, Y. Liu, G. Li, J. Guo, H. Lu, Z. Guo, *Nat. Commun.* **2021**, *12*, 6606.
[51] X. Wang, J. Meng, X. Lin, Y. Yang, S. Zhou, Y. Wang, A. Pan, *Adv. Funct. Mater.* **2021**, *31*, 2106114.
[52] J. Wang, K. K. Manga, Q. Bao, K. P. Loh, *J. Am. Chem. Soc.* **2011**, *133*, 8888.
[53] M. Chen, Z. Xia, Q. Liu, *Inorg. Chem.* **2016**, *55*, 11316.
[54] J. Self, K. D. Fong, K. A. Persson, *ACS Energy Lett.* **2019**, *4*, 2843.
[55] K. H. Kucharzyk, R. L. Crawford, B. Cosens, T. F. Hess, *J. Environ. Manage.* **2009**, *91*, 303.
[56] B. Kang, H. Tang, Z. Zhao, S. Song, *ACS Omega* **2020**, *5*, 6229.
[57] F. Ming, Y. Zhu, G. Huang, A.-H. Emwas, H. Liang, Yi Cui, H. N. Alshareef, *J. Am. Chem. Soc.* **2022**, *144*, 7160.
[58] S. Zhang, M. Ye, Y. Zhang, Y. Tang, X. Liu, C. C. Li, *Adv. Funct. Mater.* **2023**, *33*, 2208230.
[59] L. Hong, X. Wu, Y.-S. Liu, C. Yu, Y. Liu, K. Sun, C. Shen, W. Huang, Y. Zhou, J.-S. Chen, K.-X. Wang, *Adv. Funct. Mater.* **2023**, *33*, 2300952.
[60] Y. Fang, X. Xie, B. Zhang, Y. Chai, B. Lu, M. Liu, J. Zhou, S. Liang, *Adv. Funct. Mater.* **2022**, *32*, 2109671.
[61] J. Gao, X. Xie, S. Liang, B. Lu, J. Zhou, *Nano-Micro Lett.* **2021**, *13*, 69.
[62] H. Qiu, X. Du, J. Zhao, Y. Wang, J. Ju, Z. Chen, Z. Hu, D. Yan, X. Zhou, G. Cui, *Nat. Commun.* **2019**, *10*, 5374.
[63] Y. Wang, T. Wang, D. Dong, J. Xie, Y. Guan, Y. Huang, J. Fan, Y.-C Lu, *Matter* **2022**, *5*, 162.
[64] J.-B. Brubach, A. Mermet, A. Filabozzi, A. Gerschel, P. Roy, *J. Chem. Phys.* **2005**, *122*, 184509.
[65] T. Petit, L. Puskar, T. Dolenko, S. Choudhury, E. Ritter, S. Burikov, K. Laptinskiy, Q. Brzustowski, U. Schade, H. Yuzawa, M. Nagasaka, N. Kosugi, M. Kurzyp, A. Venerosy, H. Girard, J.-C. Arnault, E. Osawa, N. Nunn, O. Shenderova, E F. Aziz, *J. Phys. Chem. C* **2017**, *121*, 5185.
[66] K. Morokuma, *J. Chem. Phys.* **2003**, *55*, 1236.
[67] F. Wang, O. Borodin, T. Gao, X. Fan, W. Sun, F. Han, A. Faraone, J. A. Dura, K. Xu, C. Wang, *Nature Mater.* **2018**, *17*, 543.
[68] F. Wang, O. Borodin, M. S. Ding, M. Gobet, J. Vatamanu, X. Fan, T. Gao, N. Eidson, Y. Liang, W. Sun, S. Greenbaum, K. Xu, C. Wang, *Joule* **2018**, *2*, 927.
[69] N. Dubouis, A. Serva, E. Salager, M. Deschamps, M. Salanne, A. Grimaud, *J. Phys. Chem. Lett.* **2018**, *9*, 6683.
[70] Y. Yokoyama, T. Fukutsuka, K. Miyazaki, T. Abe, *J. Electrochem. Soc.* **2018**, *165*, A3299.
[71] Z. Khan, D. Kumar, X. Crispin, *Adv. Mater.* **2023**, *35*, 2300369.
[72] A. Pei, G. Zheng, F. Shi, Y. Li, Y. Cui, *Nano Lett.* **2017**, *17*, 1132.
[73] D. Y. Kwok, D. Li, A. W. Neumann, *Colloids Surf., A* **1994**, *89*, 181.
[74] L. Makkonen, *J. Phys.: Condens. Matter* **2016**, *28*, 135001.
[75] X. Yu, Z. Li, X. Wu, H. Zhang, Q. Zhao, H. Liang, H. Wang, D. Chao, F. Wang, Y. Qiao, H. Zhou, S.-G. Sun, *Joule* **2023**, *7*, 1145.
[76] Z. Cai, J. Wang, Z. Lu, R. Zhan, Y. Ou, Li Wang, M. Dahbi, J. Alami, J. Lu, K. Amine, Y. Sun, *Angew. Chem., Int. Ed. Engl.* **2022**, *61*, 202116560.
[77] M. Qiu, P. Sun, Y. Wang, L. Ma, C. Zhi, W. Mai, *Angew. Chem., Int. Ed. Engl.* **2022**, *61*, 202210979.
[78] M. Qiu, P. Sun, A. Qin, G. Cui, W. Mai, *Energy Stor. Mater.* **2022**, *49*, 463.
[79] Z. Huang, Z. Li, Y. Wang, J. Cong, X. Wu, X. Song, Y. Ma, H. Xiang, Y. Huang, *ACS Energy Lett.* **2023**, *8*, 372.
[80] J. Wan, R. Wang, Z. Liu, L. Zhang, F. Liang, T. Zhou, S. Zhang, L. Zhang, Q. Lu, C. Zhang, Z. Guo, *ACS Nano* **2023**, *17*, 1610.
[81] Y. Zhu, J. Yin, X. Zheng, A.-H. Emwas, Y. Lei, O F. Mohammed, Y. Cui, H. N. Alshareef, *Energy Environ. Sci.* **2021**, *14*, 4463.
[82] T. Wei, Q. Li, G. Yang, C. Wang, *Adv. Energy Mater.* **2019**, *9*, 1901480.
[83] Z. Wang, M. Zhou, L. Qin, M. Chen, Z. Chen, S. Guo, L. Wang, G. Fang, S. Liang, *eScience* **2022**, *2*, 209.
[84] H. J. Kim, S. Kim, K. Heo, J.-H. Lim, H. Yashiro, S.-T. Myung, *Adv. Energy Mater.* **2023**, *13*, 2203189.
[85] P. Xiong, Y. Kang, N. Yao, X. Chen, H. Mao, W.-S. Jang, D M. Halat, Z.-H. Fu, M.-H. Jung, H. Y Jeong, Y.-M. Kim, J. A. Reimer, Q. Zhang, H. S. Park, *ACS Energy Lett.* **2023**, *8*, 1613.

© 2023 Wiley-VCH GmbH

16163028, 0, Downloaded from https://onlinelibrary.wiley.com/doi/10.1002/adfm.202311271 by Northwestern University Libraries, Wiley Online Library on [15/12/2023]. See the Terms and Conditions (https://onlinelibrary.wiley.com/terms-and-conditions) on Wiley Online Library for rules of use; OA articles are governed by the applicable Creative Commons License

[86] J. Winiarski, W. Tylus, K. Winiarska, I. Szczygiel, B. Szczygiel, *J. Spectrosc.* **2018**, *2018*, 2079278.
[87] J. Hao, B. Li, X. Li, X. Zeng, S. Zhang, F. Yang, S. Liu, D. Li, C. Wu, Z. Guo, *Adv. Mater.* **2020**, *32*, 2003021.
[88] A. Wang, Li Wang, Y. Wu, Y. He, D. Ren, Y. Song, B. Zhang, H. Xu, X. He, *Adv. Energy Mater.* **2023**, *13*, 2300626.
[89] D. Kundu, S. Hosseini Vajargah, L. Wan, B. Adams, D. Prendergast, L. F. Nazar, *Energy Environ. Sci.* **2018**, *11*, 881.
[90] Q. Yang, L. Li, T. Hussain, D. Wang, L. Hui, Y. Guo, G. Liang, X. Li, Z. Chen, Z. Huang, Y. Li, Y. Xue, Z. Zuo, J. Qiu, Y. Li, C. Zhi, *Angew. Chem., Int. Ed. Engl.* **2022**, *61*, 202112304.
[91] E. Peled, S. Menkin, *J. Electrochem. Soc.* **2017**, *164*, A1703.
[92] P. He, G. Zhang, X. Liao, M. Yan, X. Xu, Q. An, J. Liu, L. Mai, *Adv. Energy Mater.* **2018**, *8*, 1702463.
[93] R. Yuksel, O. Buyukcakir, W. K. Seong, R. S. Ruoff, *Adv. Energy Mater.* **2020**, *10*, 1904215.
[94] K. Wang, J. Wang, P. Chen, M. Qin, C. Yang, W. Zhang, Z. Zhang, Y. Zhen, F. Fu, B. Xu, *Small* **2023**, *19*, 2300585.
[95] F. Wan, L. Zhang, X. Dai, X. Wang, Z. Niu, J. Chen, *Nat. Commun.* **2018**, *9*, 1656.
[96] Z. Wang, J. Diao, J. N. Burrow, K. K. Reimund, N. Katyal, G. Henkelman, C. B. Mullins, *Adv. Funct. Mater.* **2023**, 2304791.
[97] Z. Zhang, T. Yao, E. Wang, B. Sun, K. Sun, Z. Peng, *ACS Appl. Mater. Interfaces* **2022**, *14*, 45484.
[98] Y. Sun, H. Ma, X. Zhang, B. Liu, L. Liu, X. Zhang, J. Feng, Q. Zhang, Y. Ding, B. Yang, L. Qu, X. Yan, *Adv. Funct. Mater.* **2021**, *31*, 2101277.
[99] Q. Li, D. Lu, J. Zheng, S. Jiao, L. Luo, C.-M. Wang, K. Xu, J.-G Zhang, W. Xu, *ACS Appl. Mater. Interfaces* **2017**, *9*, 42761.
[100] Z. Xing, G. Xu, X. Xie, M. Chen, B. Lu, J. Zhou, S. Liang, *Nano Energy* **2021**, *90*, 106621.
[101] Z. Yang, W. Li, Q. Zhang, C. Xie, H. Ji, Y. Tang, Y. Li, H. Wang, *Mater. Today Energy* **2022**, *28*, 101076.
[102] X. Dong, Y. Lin, P. Li, Y. Ma, J. Huang, D. Bin, Y. Wang, Y. Qi, Y. Xia, *Angew. Chem., Int. Ed. Engl.* **2019**, *58*, 5623.

 © 2023 Wiley-VCH GmbH

16163028, 0, Downloaded from https://onlinelibrary.wiley.com/doi/10.1002/adfm.202311271 by Northwestern University Libraries, Wiley Online Library on [15/12/2023]. See the Terms and Conditions (https://onlinelibrary.wiley.com/terms-and-conditions) on Wiley Online Library for rules of use; OA articles are governed by the applicable Creative Commons License